Paleoseismic Trenching Reveals Late Quaternary Kinematics of the Leech River Fault: Implications for Forearc Strain Accumulation in Northern Cascadia

Nicolas Harrichhausen*[1], Kristin D. Morell[1], Christine Regalla[2], Scott E. K. Bennett[3], Lucinda J. Leonard[4], Emerson M. Lynch[2], and Edwin Nissen[4]

ABSTRACT

New paleoseismic trenching indicates late Quaternary oblique right-lateral slip on the Leech River fault, southern Vancouver Island, Canada, and constrains permanent forearc deformation in northern Cascadia. A south-to-north reduction in northward Global Navigation Satellite System velocities and seismicity across the Olympic Mountains, Strait of Juan de Fuca (JDF), and the southern Strait of Georgia, has been used as evidence for permanent north–south crustal shortening via thrust faulting between a northward migrating southern forearc and rigid northern backstop in southwestern Canada. However, previous paleoseismic studies indicating late Quaternary oblique right-lateral slip on west-northwest-striking forearc faults north of the Olympic Mountains and in the southern Strait of Georgia are more consistent with forearc deformation models that invoke oroclinal bending and(or) westward extrusion of the Olympic Mountains. To help evaluate strain further north across the Strait of JDF, we present the results from two new paleoseismic trenches excavated across the Leech River fault. In the easternmost Good Hope trench, we document a vertical fault zone and a broad anticline deforming glacial till. Comparison of till clast orientations in faulted and undeformed glacial till shows evidence for postdeposition faulted till clast rotation, indicating strike-slip shear. The orientation of opening mode fissuring during surface rupture is consistent with right-lateral slip and the published regional $S_{H\max}$ directions. Vertical separation and the formation of scarp-derived colluvium along one fault also indicate a dip-slip component. Radiocarbon charcoal dating within offset glacial till and scarp-derived colluvium suggest a single surface rupturing earthquake at 9.4 ± 3.4 ka. The oblique right-lateral slip sense inferred in the Good Hope trench is consistent with slip kinematics observed on other regional west-northwest-striking faults and indicates that these structures do not accommodate significant north–south shortening via thrust faulting.

KEY POINTS

- We constrain the late Quaternary kinematics of the Leech River fault in the northern Cascadia forearc.
- The Leech River fault hosted a Holocene surface rupturing earthquake, with oblique right-lateral slip.
- This structure is a part of a network of strike-slip faults that accommodates oroclinal bending of the forearc.

Supplemental Material

INTRODUCTION

The styles, rates, and distribution of forearc deformation provide information on the mechanisms of strain partitioning between the megathrust and overriding crust (e.g., Wells *et al.*, 2003; Chlieh *et al.*, 2008; Saillard *et al.*, 2017) and the stress state and strength of the forearc and megathrust within

1. Department of Earth Science, University of California, Santa Barbara, Santa Barbara, California, U.S.A.; 2. School of Earth and Sustainability, Northern Arizona University, Flagstaff, Arizona, U.S.A.; 3. U.S. Geological Survey, Geology, Minerals, Energy, and Geophysics Science Center, Portland, Oregon, U.S.A.; 4. School of Earth and Ocean Sciences, University of Victoria, Victoria, British Columbia, Canada

*Corresponding author: nharrichhausen@ucsb.edu

Cite this article as Harrichhausen, N., K. D. Morell, C. Regalla, S. EK. Bennett, L. J. Leonard, E. M. Lynch, and E. Nissen (2021). Paleoseismic Trenching Reveals Late Quaternary Kinematics of the Leech River Fault: Implications for Forearc Strain Accumulation in Northern Cascadia, *Bull. Seismol. Soc. Am.* **XX**, 1–29, doi: 10.1785/0120200204

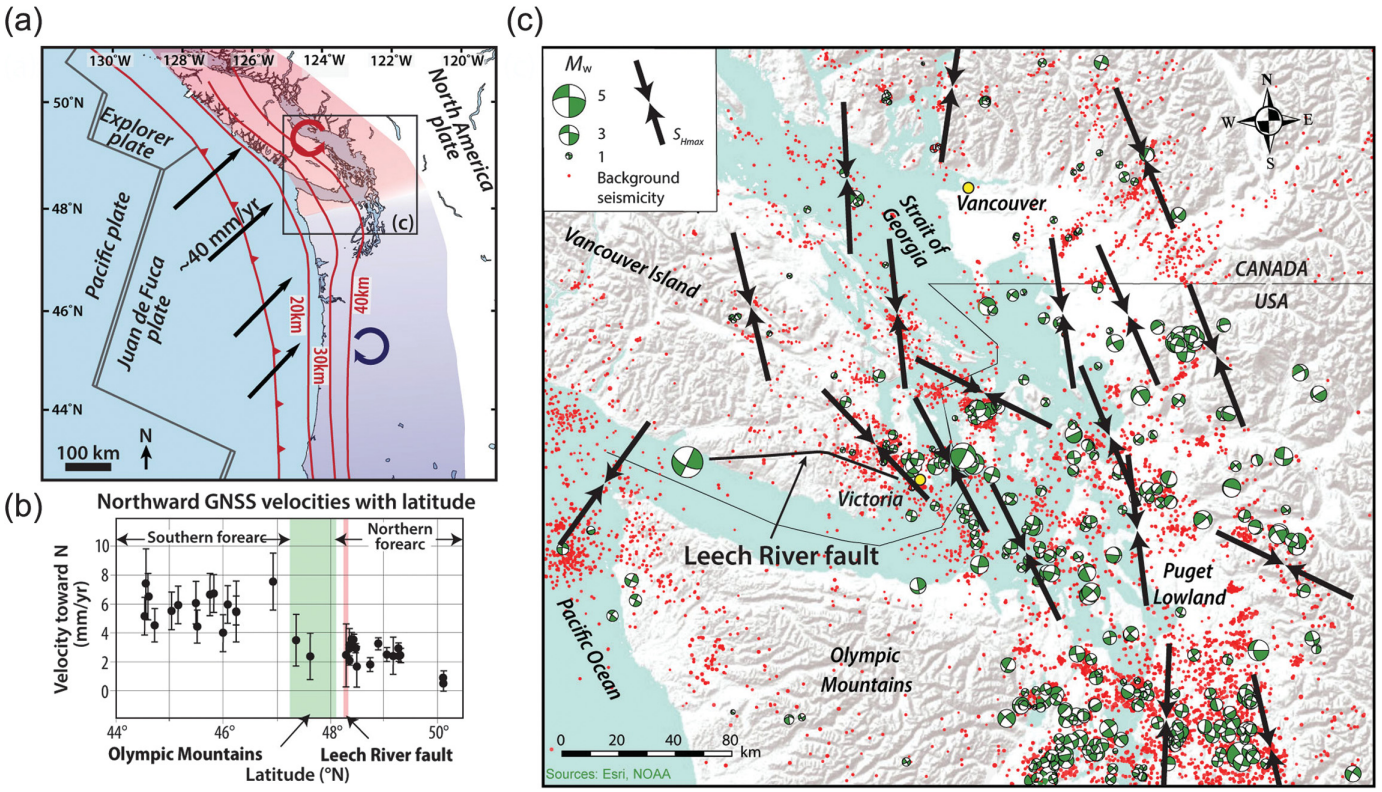

Figure 1. (a) Map showing the tectonic setting of Cascadia. Juan de Fuca (JDF) plate motion with respect to North America (NA) (DeMets *et al.*, 2010) shown in thick black arrows. Red lines are contours of depth to the subducting slab (McCrory *et al.*, 2012). Clockwise rotation of southern Cascadia (blue) and counterclockwise rotation of northern Cascadia (red) with respect to stable NA is adapted from Finley *et al.* (2019). (b) Northward component of Global Navigation Satellite System (GNSS) velocities from the onshore inner forearc as a function of latitude. GNSS data are from Mazzotti *et al.* (2002). (c) Upper plate crustal seismicity (<35 km depth) in northern Cascadia from 1 January 1970 to 29 April 2015. Compiled by Brocher *et al.* (2017) from the Pacific Northwest Seismic Network/Advanced National Seismic system. $S_{H\,max}$ directions calculated from clusters of crustal earthquake focal mechanisms (Balfour *et al.*, 2011) are shown with black arrow pairs.

subduction zones (e.g., Wang *et al.*, 2019). However, the processes that produce the varying styles of forearc strain over many seismic cycles remain incompletely understood.

Studies of the spatial distribution, kinematics, and rates of slip on active upper plate fault systems can help constrain the conditions and mechanisms responsible for the disparate types of forearc strain observed globally. For example, regional uplift paired with extensional faulting in Crete, Greece, suggests that uplift in the Central Hellenic forearc is caused by underplating at the down-dip edge of the locked portion of the subduction zone (Gallen *et al.*, 2014). In addition, normal faults in the forearc of northern Chile accommodate margin perpendicular extension through a combination of coseismic elastic rebound, subduction erosion, and interseismic flexure of the upper crust (Allmendinger and González, 2010). Finally, geologic and geomorphic mapping shows that formation and uplift of the Fila Costeña thrust belt in the inner forearc of the Middle America subduction zone is controlled by the subduction of the overthickened crust of the Cocos ridge (Sitchler *et al.*, 2007; Morell *et al.*, 2013).

At the Cascadia subduction zone, paleoseismic data from active forearc faults in Oregon and Washington state suggest that vertical axis forearc rotation (Fig. 1a; Finley *et al.*, 2019) and forearc sliver migration (Fig. 1b; Wells *et al.*, 1998; Wang *et al.*, 2003; Sherrod *et al.*, 2013) are the driving forces of forearc deformation, but these mechanisms in the northern forearc near the United States–Canada border are less well understood. Northward migration and clockwise rotation of the southern Cascadia forearc relative to stable North America (NA) are at least partially accommodated by a network of predominately northwest–southeast-striking oblique faults in Oregon and southwest Washington (Blakely *et al.*, 2000; Brocher *et al.*, 2017; Wells *et al.*, 2020) and east-west-striking folds and thrust faults in the Puget Lowland (Fig. 2; Johnson *et al.*, 1994; Brocher *et al.*, 2001; Blakely *et al.*, 2002, 2011). However, how forearc strain is accommodated north of the Olympic Mountains and the Puget Lowland remains a topic of debate (e.g., Wells *et al.*, 1998; Finley *et al.*, 2019).

Here, we examine the late Quaternary kinematics and slip history of the Leech River fault on southern Vancouver Island, British Columbia, Canada. This active forearc structure (Morell *et al.*, 2017, 2018) lies in a key region where geodetic and seismicity studies suggest that forearc strain may decrease northward along the strike of the subducting slab (Fig. 1b;

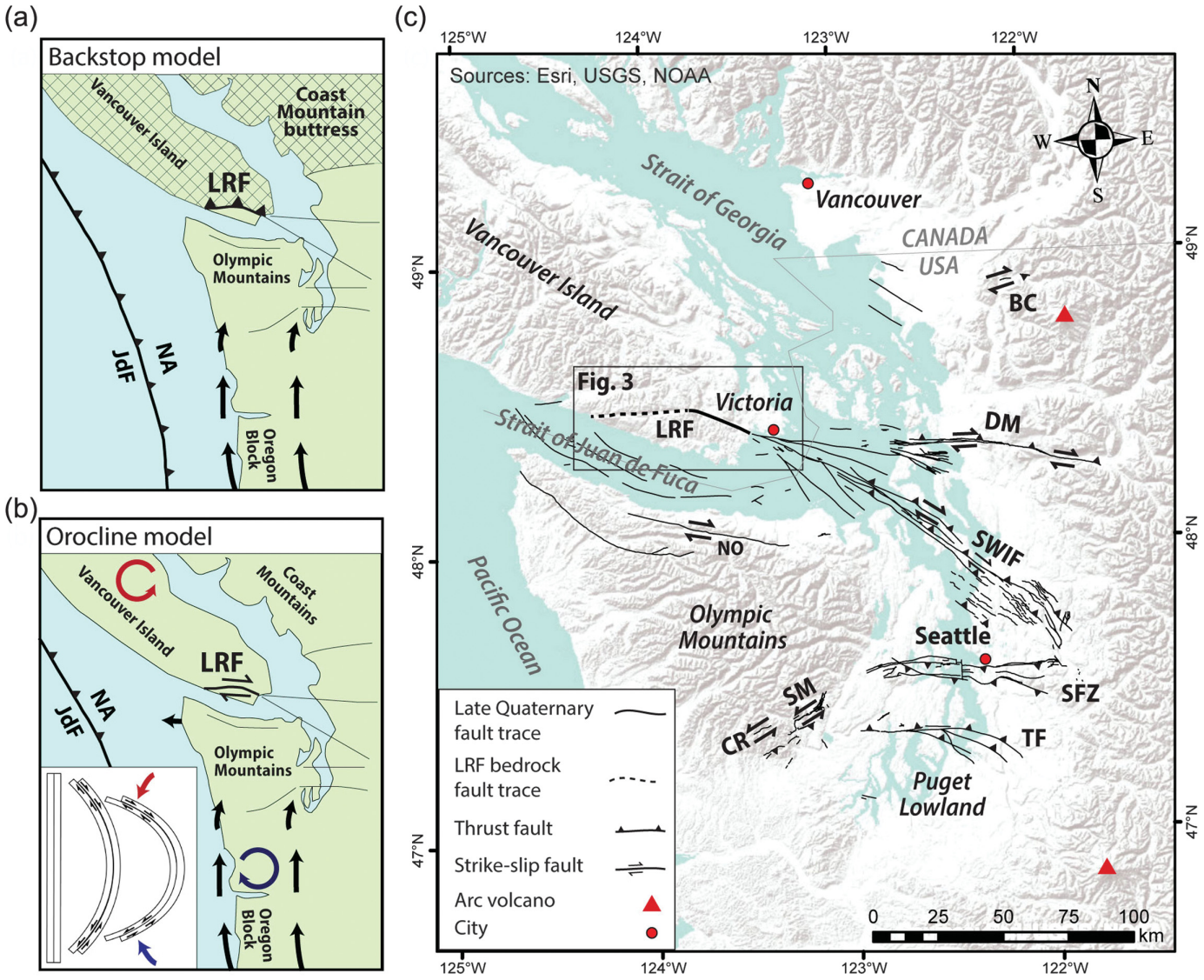

Figure 2. Schematic of alternative permanent forearc deformation models and map of late Quaternary–Active fault traces in northern Cascadia. (a,b) Black arrows show forearc motion with respect to stable NA, and red and blue arrows show counterclockwise and clockwise rotation, respectively, of the northern and southern Cascadia forearc. Thin black lines are the approximate surface traces of late Quaternary faults shown in (c). (a) "Backstop" model: Northward migration of the Oregon block is accommodated by north–south shortening in western Washington State and southern Vancouver Island due to collision with the Canadian Coast Mountains acting as a rigid buttress (hatched region), which would induce thrust faulting on the Leech River fault (LRF). (b) "Orocline" model: Northward migration of the Oregon block is accommodated by oroclinal bending of the Cascadia forearc, which would induce right-lateral slip on the LRF as a result of flexural slip on the northern limb of the orocline (see inset). Contemporaneous left-lateral slip on faults south of the Olympic Mountains, as a result of flexural slip on the southern limb of the orocline, would permit westward escape of the Olympic Peninsula. (c) Late Quaternary-active fault traces in the northern Cascadia forearc from the U.S. Geological Survey (USGS) Quaternary fold, and fault database for the United States. Selected faults show slip sense: Canyon River (CR) and Saddle Mountain (SM) faults (Wilson *et al.*, 1979; Walsh *et al.*, 1997; Walsh and Logan, 2007; Witter *et al.*, 2008; Blakely *et al.*, 2009; Barnett *et al.*, 2015; Bennett *et al.*, 2017), Seattle fault zone (SFZ) (Johnson *et al.*, 1994, 1999; Blakely *et al.*, 2002; Nelson *et al.*, 2003), Tacoma fault zone (TF) (Sherrod *et al.*, 2004), North Olympic (NO) fault zone (Nelson *et al.*, 2017; Schermer *et al.*, 2020), southern Whidbey Island fault zone (SWIF) (Johnson *et al.*, 1996; Sherrod *et al.*, 2008), Boulder Creek fault (BC) (Sherrod *et al.*, 2013), Devils Mountain fault (DM) (Johnson *et al.*, 2001; Personius *et al.*, 2014; Barrie and Greene, 2018). The LRF is an along-strike continuation of the Devils Mountain fault and southern Whidbey Island fault zone.

Mazzotti *et al.*, 2002; Balfour *et al.*, 2011), and where the forearc transitions from active uplift of the Olympic Mountains (e.g., Brandon *et al.*, 1998; Adams and Ehlers, 2017) to the less seismically active Canadian forearc. We use paleoseismic trenching and structural and geomorphic mapping to determine the timing, extent, and kinematics of Quaternary ruptures on the Leech River fault. We explore the implications for how networks of crustal faults accommodate forearc strain and consider the resulting seismic hazard to nearby population centers.

TECTONIC SETTING

Along the Cascadia subduction zone, the Juan de Fuca plate subducts toward the northeast beneath the NA plate (Fig. 1a). At the latitude of the Leech River fault, Global Navigation Satellite System (GNSS) data, paleomagnetic data, and instrumental seismicity suggest several margin-parallel variations in strain accumulation of the onshore Cascadia forearc. First, GNSS surface velocities with respect to stable NA (Miller *et al.*, 2001; Mazzotti *et al.*, 2003; McCaffrey *et al.*, 2007; Finley *et al.*, 2019) and paleomagnetic rotations (e.g., Prothero *et al.*, 2008; Wells and McCaffrey, 2013) show opposing senses of forearc rotation north and south of the Olympic Mountains, accordant with oroclinal bending from 18 Ma to the present day (Fig. 1a; Wells and McCaffrey, 2013; Finley *et al.*, 2019). Second, residual GNSS velocities, in which elastic deformation resulting from coupling along the megathrust is removed, suggest westward extrusion of the forearc relative to stable NA near the Olympic Mountains (Mazzotti *et al.*, 2002, 2011). Finally, across the Olympics, there is a south-to-north reduction in the northward component of forearc GNSS velocities that requires net north–south crustal shortening (Fig. 1b; Khazaradze *et al.*, 1999; Mazzotti *et al.*, 2002). This observation is supported by instrumental crustal seismicity, which is clustered in the Puget Lowland and the southern Strait of Georgia and diminishes significantly north of the Leech River fault (Fig. 1c; Brocher *et al.*, 2017). Focal mechanisms from this data primarily indicate right-lateral slip on west-northwest-striking faults or left-lateral slip on south-southwest-striking faults, and north–south shortening on reverse faults (Fig. 1c; Brocher *et al.*, 2017; Li *et al.*, 2018). The maximum horizontal compressive stress ($S_{H\,\mathrm{max}}$) directions derived from this seismicity are directed north–south to northwest–southeast (Balfour *et al.*, 2011), parallel to the margin and consistent with the north–south shortening predicted from the GNSS velocity gradient (Fig. 1b,c).

Models for permanent forearc deformation in northern Cascadia

Two models of permanent forearc deformation have been proposed to accommodate the north–south-oriented margin-parallel shortening in the upper crust near the Olympic Mountains and southern Vancouver Island. In the "backstop" model, the Canadian Coast Mountains act as a barrier against a northward migrating southern Cascadia forearc sliver, known as the Oregon block (Fig. 2a; Wells *et al.*, 1998; Wang *et al.*, 2003; Sherrod *et al.*, 2013). Considering the west-northwest strike of the Leech River fault, north–south shortening of the upper crust on southern Vancouver Island against a rigid buttress to the north predicts reverse slip sense on the Leech River fault, similar to the Seattle and Tacoma faults in the Puget Lowland (Fig. 2c; Johnson *et al.*, 1994, 1999; Nelson *et al.*, 2003; Blakely *et al.*, 2002; Sherrod *et al.*, 2004).

In the second "orocline" model, active strike-slip faults surrounding the Olympic Mountains instead accommodate deformation induced by oroclinal bending (Fig. 2b). Finley *et al.* (2019) suggest that right-lateral west-northwest-striking faults to the north of (including the Leech River fault) and left-lateral west-southwest-striking faults to the south of the Olympic Mountains accommodate deformation analogous to flexural slip on the limbs of the orocline (e.g., Fig. 2b; Donath and Parker, 1964; Babaahmadi and Rosenbaum, 2015), with shortening, uplift, and westward extrusion occurring within the core of the Olympic Mountains (e.g., Brandon and Calderwood, 1990; Brandon *et al.*, 1998; Batt *et al.*, 2001; Pazzaglia and Brandon, 2001; Adams and Ehlers, 2017; Nelson *et al.*, 2017; Michel *et al.*, 2018). The accompanying westward extrusion may also induce right-lateral and left-lateral faulting north and south of the Olympic Mountains, respectively (e.g., Nelson *et al.*, 2017). This model is compatible with paleoseismic studies of regional Holocene-active fault kinematics (e.g., Sherrod *et al.*, 2008; Personius *et al.*, 2014; Barnett *et al.*, 2015; Nelson *et al.*, 2017; Schermer *et al.*, 2020) that show oblique left-lateral and right-lateral faults south and north, respectively, of the Olympic Mountains (Fig. 2c).

In this study, we examine the late Quaternary kinematics of the Leech River fault in the context of these tectonic models by testing whether this structure has accommodated reverse slip (Fig. 2a), or, instead, it has hosted oblique or strike-slip faulting (Fig. 2b).

Previous paleoseismic studies of the Leech River fault

The Leech River fault, which separates the Mesozoic Pacific Rim and Wrangellia terranes to the north against the Eocene Crescent terrane to the south (Fig. 3; MacLeod *et al.*, 1977; Muller, 1977; Fairchild and Cowan, 1982; Massey *et al.*, 2005), has been traditionally considered to be last active as a thrust (Clowes *et al.*, 1987) or oblique left-lateral fault (Fairchild and Cowan, 1982) in the Eocene to Oligocene. However, several recent studies that combined geologic and geomorphic mapping with paleoseismic trenching suggest that the Leech River fault has hosted surface-rupturing earthquakes in the late Quaternary. Mapping of an ~60 km long, ~1 km wide fault zone formed in late Quaternary glacial sediment suggests that faulting postdates the last glaciation ~13,100 calendar years before 1950 (cal B.P.) (Fig. 4; Morell *et al.*, 2017; Graham, 2018). Paleoseismic trenching across a fault scarp developed in Holocene-aged loess and colluvium revealed stratigraphic and structural evidence for three surface rupturing earthquakes at 1.7 ± 0.1, 2.2 ± 0.1, and 8.7 ± 0.3 ka (Morell *et al.*, 2018).

Late Quaternary right-lateral slip on the Leech River fault is suggested by seismicity and paleoseismic investigations of along-strike fault systems. Oblique right-lateral slip during Holocene surface rupturing earthquakes is observed in paleoseismic trenches on both the Devils Mountain and southern

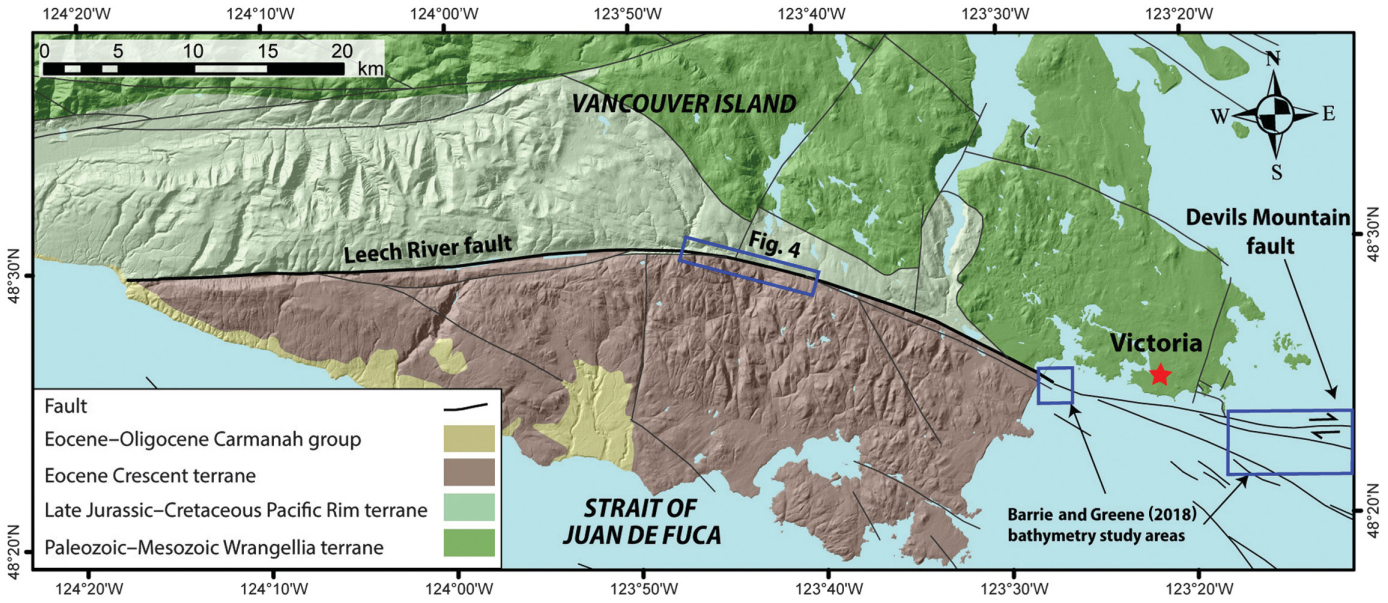

Figure 3. Geologic terrane map of southern Vancouver Island highlighting the Leech River fault, which juxtaposes the Pacific Rim and Wrangellia terrane from the Crescent terrane. Right-lateral slip on the Devils Mountain fault, the offshore continuation of the Leech River fault, is from Barrie and Greene (2018) and Personius *et al.* (2014). Geology adapted from Massey *et al.* (2005). Blue boxes show locations of Figure 4 and Barrie and Greene (2018) study locations.

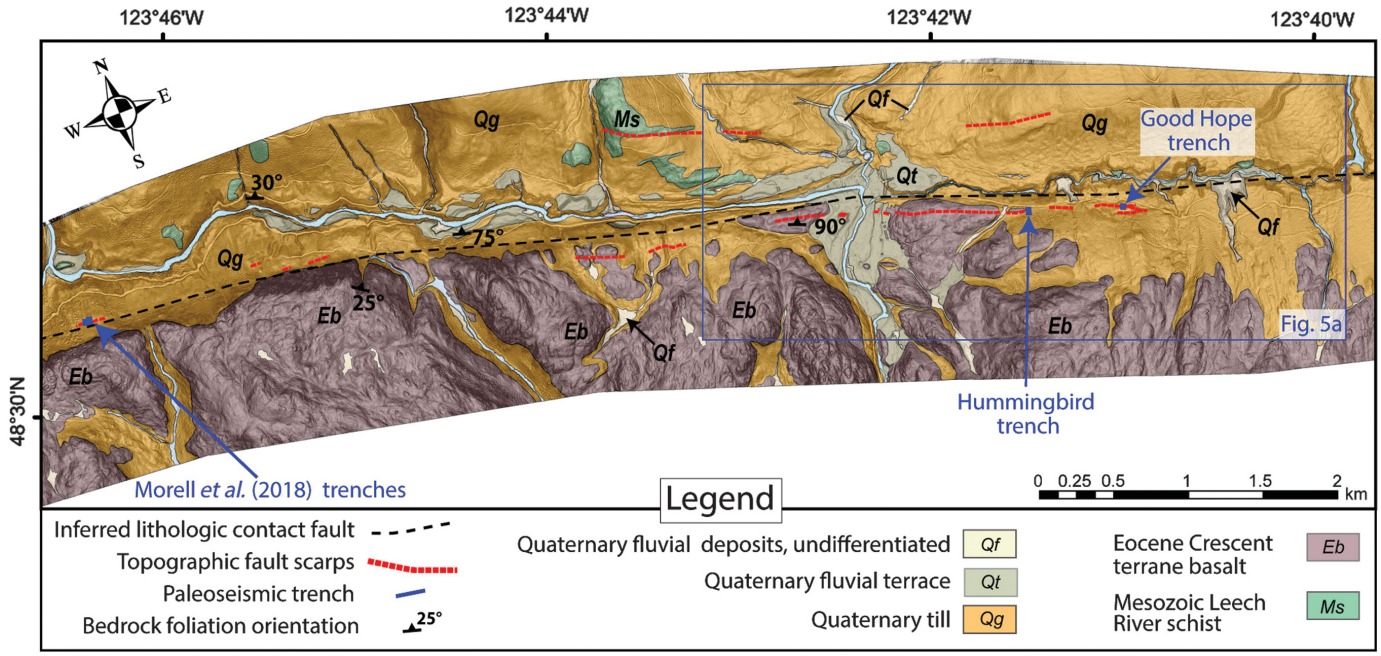

Figure 4. Surficial geologic map of the central Leech River fault showing locations of the paleoseismic trenches from this study (Good Hope and Hummingbird) and from Morell *et al.* (2018). Figure 5a location shown with blue box. Surficial geology and lithological contact fault adapted from Massey *et al.* (2005), Morell *et al.* (2017), and Graham (2018).

Whidbey Island fault systems (Johnson *et al.*, 1996; Sherrod *et al.*, 2008; Personius *et al.*, 2014), which appear to merge with the Leech River fault along strike (Fig. 2). These results are consistent with right-lateral offset of Holocene submarine landforms along the offshore portion of the Devils Mountain fault (Barrie and Greene, 2018), only ~10 km east

of the Leech River fault (Fig. 3). These paleoseismic results also agree with kinematic results from microseismicity studies, which exhibit primarily right-lateral focal mechanisms along the trace of the Leech River fault (Li *et al.*, 2018).

Although these data sets argue for right-lateral slip of the Leech River fault throughout the late Quaternary, some of the recent paleoseismic studies argue for dip-slip surface rupturing earthquakes. Deformed postglacial channel thalwegs and interfluves at the previous paleoseismic trenches on the Leech River fault (Fig. 4) exhibit little to no lateral offset, arguing for predominantly dip-slip late Quaternary surface ruptures (Morell *et al.*, 2017). These observations are consistent with kinematic indicators (e.g., slickenlines and colluvial wedge development) in the paleoseismic trenches that show three dip-slip surface rupturing earthquakes.

Discrepancies in Holocene sense of slip, determined from studies on and nearby the Leech River fault, may be due to complex strike-slip surface ruptures, which highlight the need to obtain fault kinematics from additional locations on the fault. Studies show that measurements from a single transect or single trench may not be representative of the predominant kinematics of a single rupture sequence (e.g., 2016 M_w 7.0 Kumamoto earthquake, Toda *et al.*, 2016). To help address the difference between the observed dip-slip surface rupture on the Leech River fault (Morell *et al.*, 2017, 2018), and right-lateral fault kinematics observed in seismicity data (Li *et al.*, 2018) and paleoseismic data from faults along strike (Johnson *et al.*, 1996; Sherrod *et al.*, 2008; Personius *et al.*, 2014; Greene *et al.*, 2018), we place new constraints on the kinematics of the Leech River fault by analysis of this structure at multiple locations along its surface trace.

METHODS

We use a combination of light detection and ranging (lidar)-based geomorphic mapping and paleoseismic trenching to document the presence of surface ruptures and evaluate the timing and kinematics of displacement. The use of these methods in northern Cascadia has proven successful in overcoming challenges presented by (1) dense vegetation, which can obscure fault-related features; (2) relatively slow rates of crustal deformation, which may be associated with long earthquake recurrence intervals (e.g., <1 mm/yr, McCaffrey *et al.*, 2007); and (3) the recent continental glaciation ~13,100 cal B.P. (Armstrong *et al.*, 1965; Alley and Chatwin, 1979) that has resulted in a limited thickness and stratigraphic extent of the late Quaternary sedimentary record (e.g., Personius *et al.*, 2014).

We excavated two paleoseismic trenches—the Good Hope and Hummingbird trenches—7 km east–southeast of previous paleoseismic trenching sites on the Leech River fault (Morell *et al.*, 2018) and 25 km west of the city of Victoria, British Columbia (Fig. 3), to characterize late Quaternary fault kinematics at multiple points along strike of the fault. We chose the location of our paleoseismic trenches based on surficial geology mapping (adapted from Graham, 2018) and new topographic analysis of fault scarps that we conducted using 2 m resolution digital elevation models (DEMs) derived from bare-Earth lidar ground returns with an estimated vertical precision of 10 cm (James *et al.*, 2010). We used several criteria to determine if these scarps were of tectonic origin including: their location parallel with and along strike of previously mapped brittle faulting in Eocene bedrock, continuity of scarps across other topographic features, their location away from obvious human-made geomorphic features, and whether scarps exhibited vertical separation of a previously continuous surface. We used a Monte Carlo routine to estimate vertical separation, based on different possible surface regressions on the slopes above and below the topographic scarp (e.g., Thompson *et al.*, 2002). The uncertainty is based on a 95% confidence interval of the results of the Monte Carlo routine.

The trenches were excavated and logged in the summer of 2018. The Good Hope trench was ~17 m long, the Hummingbird trench was ~39 m long, and both trenches were ~1 m wide and up to ~2 m deep. After excavation, we set up a 1×1 m reference grid on each wall using a level and measuring tape. Digital photographs of each wall were then taken with enough overlap to create orthorectified photomosaics using Agisoft PhotoScan software (e.g., Reitman *et al.*, 2015), and these photomosaics were used as base maps for digital trench logging on tablets. Large-format high-resolution trench logs with photomosaics for the Good Hope and Hummingbird trenches are provided in the supplemental material (Figs. S1–S4).

We measured and statistically analyzed orientations of glacial till clasts within and outside of fault zones to characterize the location and style of faulting in the Good Hope trench. Given previous experimental (e.g., Hooyer and Iverson, 2000; Carr and Rose, 2003; Thomason and Iverson, 2006) and field (e.g., Dowdeswell and Sharp, 1986; Ham and Mickelson, 1994; Carr and Rose, 2003) observations, we expect the long axis of prolate clasts in undeformed lodgment till to trend parallel to, and plunge opposite the flow direction of, the overriding ice. In undeformed meltout till, we expect the a/b planes of oblate clasts to lie parallel to their plane of deposition (Boulton, 1971), unless they were imbricated during resedimentation. In contrast, in faulted lodgment till, we expect the long-axis orientations of prolate clasts to either deviate from the mean clast orientation of undeformed till, or to rotate into parallelism with fault-related shear (e.g., Cladouhos, 1999). In faulted meltout till, we also expect to observe oblate clasts rotated into parallelism with fault-related shear or random clast orientations representing a lack of imbrication.

We collected lineation measurements of 50 clasts in undeformed lodgment till and 75 clasts from within the fault zones formed in lodgment till. We also collected attitudes of a/b planes of 55 clasts in undeformed meltout till and 50 clasts from the inferred fault zones formed in meltout till. We used Past 3 software (Hammer *et al.*, 2001) to perform Bingham tests (Bingham, 1974) to examine whether each of these sample sets exhibits a

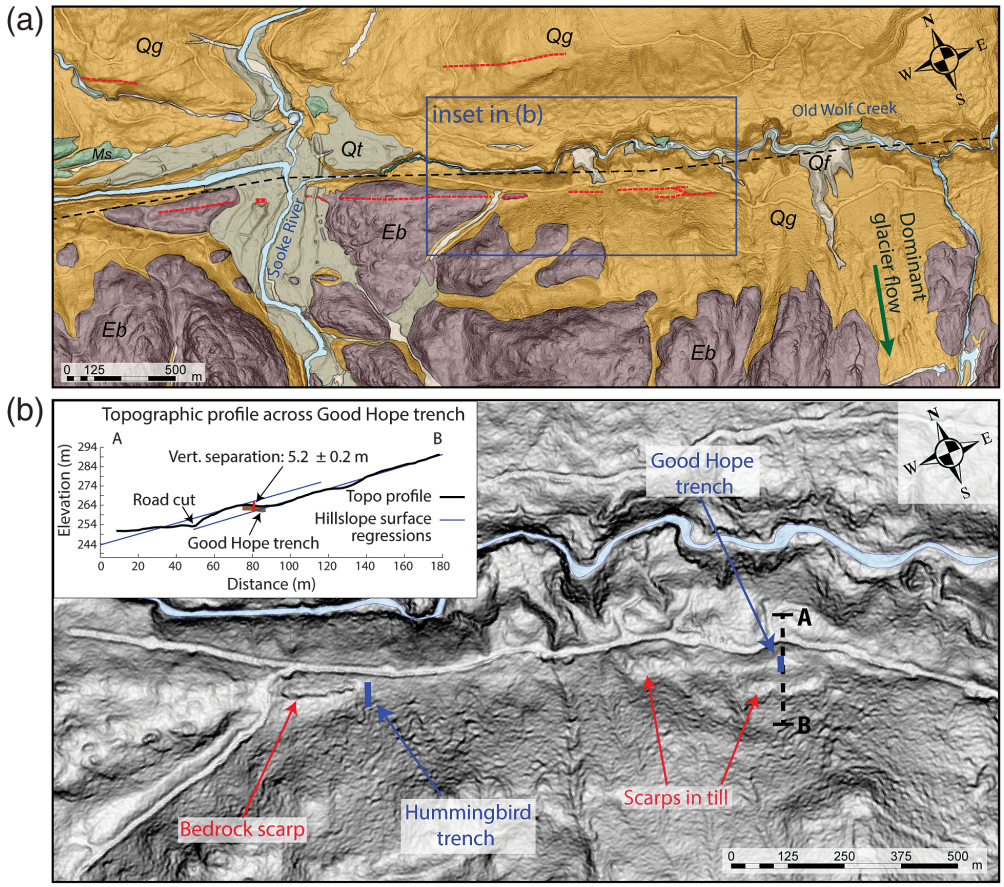

Figure 5. (a) Surficial geology draped over slope map and (b) unannotated slope map showing fault scarps and the location of the Good Hope and Hummingbird trenches (see Figs. 3 and 4 for location). Surficial geology legend is same as Figure 4. Glacier flow direction, derived from measurements of whalebacks and drumlins, is shown with a green arrow in the southeast corner of (a). Fault scarp locations (red) adapted from Morell *et al.* (2017). Inset at top left of (b) shows a topographic profile along line A–B with vertical separation of the hillslope across the fault scarp at the Good Hope trench. Uncertainties in vertical separation were calculated using a Monte Carlo routine that uses the 95% confidence interval of the surface regression through the ground surface.

population with a uniform distribution, and nonparametric Mardia–Watson–Wheeler tests (e.g., Batschelet, 1981) to examine whether the data sets were statistically different from one another. To determine the local dominant glacial flow direction within a ~4 km radius of the trenches, we identified and measured glacial flow indicators, such as drumlins and roche moutoneés, using bare-Earth lidar-derived hillshade and slope maps, and averaged the azimuths of these measurements.

We performed ^{14}C dating of 12 macroscopic charcoal samples from surficial units in the Good Hope trench to determine their ages and bracket the timing of any earthquake events. The samples were dated at the Keck Carbon Cycle AMS Laboratory in Irvine, California. OxCal (Bronk Ramsey, 2017) was used to calibrate the radiocarbon ages with the IntCal13 ^{14}C production curve (Reimer *et al.*, 2013) to determine a range of possible calendar ages reported as cal B.P. (calendar calibrated ages before 1950) (e.g., Stuiver and Reimer, 1993). We then used OxCal to incorporate all available chronological constraints, such as stratigraphic order, to trim the probability distribution of the unit ages and model the ages of the paleoearthquakes using Monte Carlo routines and Bayesian statistics (Lienkaemper and Ramsey, 2009). We report calibrated event ages from the OxCal model as the median and uncertainty, equal to 95% confidence interval, rounded to the nearest century in thousands of calendar years (ka) before 1950.

RESULTS

Glacial and tectonic geomorphology

Our study area is located along a north-facing slope to the south of a pronounced ~1–2 km wide valley that generally follows the surface trace of the Leech River fault. The slopes on either side of the valley are mainly covered by glacial till associated with the Fraser glaciation (25–10 ka, Clague and Ward, 2011), and Fraser glaciofluvial deposits dominate the valley floor (Figs. 4 and 5a; Blyth, 1997; Graham, 2018). Bedrock exposures locally outcrop in stream cuts near the valley bottom and in steep bluffs in the highlands above the valley.

Hillshade and slope maps derived from bare-Earth lidar data (Fig. 5) show numerous till and bedrock features, indicative of a dominant southerly local glacial flow direction associated with the recent Fraser glaciation. A calculation of the axial mean and standard error of 41 streamlined features, such as whalebacks, rock drumlins (e.g., Evans, 1996), and sedimentary drumlins (Table A1), determine an average glacial flow direction of 194.8° ± 2.5° (Fig. 5). These features exhibit blunt and rounded profiles at their northern ends and exhibit more gentle relief and gradually sloping forms at their southern ends. Whalebacks and drumlins occur more prominently at elevations of ~100 m above the modern river valley (Fig. 5), where less fluvial reworking has occurred than in the valley bottom.

A strand of the Leech River fault is located on the south side of the valley drained by Old Wolf Creek, which flows west toward the Sooke River (Fig. 5). The fault strand is ~100 m south of the shear zone that is the contact between schist of

the Pacific Rim terrane and basalt of the Crescent terrane (Fig. 4). This strand consists of discontinuous south-facing (uphill-facing) scarps, with vertical separation (e.g., Fig. 5b,c), formed in both bedrock and glacial deposits. The scarps are segmented and separated by discontinuities such as overlapping fault segments or gaps up to 2 km in length.

The two paleoseismic trenches were excavated perpendicular to the fault scarps on the north-facing slope in Figure 5b. We chose not to investigate any potential fault scarps on the terrace risers along the Sooke River to the west (Fig. 5a), where placer gold mining and town development in the mid-1800s (e.g., Paterson and Basque, 2006) may have disturbed sediments that would potentially record late Quaternary fault-related deformation. Vertical separation across the fault strand (Fig. 5c) and a lack of strike-slip offset of channel thalwegs and interfluves that cross the fault scarps (Fig. 5) led us to expect dip-slip surface rupture along this segment of the Leech River fault. Therefore, we determined that paleoseismic trenching perpendicular to the fault trace would have the greatest likelihood of exposing fault offset (e.g., McCalpin, 2009).

The Hummingbird trench was excavated 20 m east along strike from an ~125 m long basalt bedrock scarp that strikes 108° (Fig. 5b). The scarp is an ~0.5–3 m high south-facing cliff and consists of minor left-stepping en échelon segments that are 10–50 m long and spaced 5–10 m apart. The exposed bedrock scarp ends west of the Hummingbird trench site and continues to the east as an ~650 m long topographic bench and uphill-facing scarp developed in glacial till and hillslope-derived colluvium. The Good Hope trench is located 625 m east of the Hummingbird trench (Fig. 5b), where the south-facing scarp is ~1 m high. This northern scarp overlaps for ~100 m with another, less continuous, uphill-facing scarp located ~35 m south of the Good Hope trench and continues for ~250 m east, until it is obscured by a road cut.

We estimate 5.2 ± 0.2 m of vertical separation of the ground surface (Fig. 5c) across the fault scarp where the Good Hope trench is excavated (Fig. 5b). The surface regression of the slope uphill and to the south of the topographic scarp matches the slope of the ground surface well. The lower surface regression was calculated using only the topographic profile ~20 m north of the topographic scarp before the slope is modified by a road cut (Fig. 5c).

Good Hope trench

Stratigraphy. The Good Hope trench reveals a faulted and folded glacial stratigraphic sequence composed of four units (Fig. 6; Table 1). The stratigraphy comprises lodgment till (unit GH1) at the base of the trench, overlain by meltout till (unit GH2), scarp-derived colluvium (unit GH3), and hillslope-derived colluvium (unit GH4). Within ~0.2–1 m of the ground surface, an O–Ae–B soil horizon has developed within all units. The trench wall reference grid (Fig. 6) is used hereafter to describe specific locations within the trenches.

Unit GH1 is a consolidated diamict that we interpret as a subglacial lodgment till. This unit contains clasts ranging in size from pebbles to boulders that increase in abundance near the top of the unit. The clasts in unit GH1 are rounded and consist of a variety of lithologies, including locally sourced schist and distally sourced intrusive igneous rocks. The matrix of unit GH1 is a well-consolidated light-gray silty clay, with rare 1–5 cm thick beds of sand, which locally exhibit small (~30 cm wavelength) tight southward-verging folds that may be a result of subglacial, syn-depositional deformation. The matrix also exhibits a well-developed subhorizontal fissile fabric subparallel with clast alignment. The well-defined fissility and consolidation is typical of a till deposited under the high pressure and stress imposed by an overriding glacier (e.g., Krüger, 1979; Ham and Mickelson, 1994; Evans *et al.*, 2006), thought to be 1–2 km thick on southern Vancouver Island during the Fraser glaciation (e.g., Alley and Chatwin, 1979; Clague and James, 2002).

Unit GH2 is an unconsolidated, clast-supported diamict that we interpret as meltout till that conformably overlies unit GH1. This unit has subangular-to-subrounded pebbles, cobbles, and occasional boulders. Clasts exhibit varied lithologies, similar to those in unit GH1, among a matrix composed of medium-to-fine sand and silt. Unit GH2 is poorly stratified, but exhibits rare discontinuous lenses of well-sorted medium-to-coarse sand near the base of the unit on both walls of the trench (between 10H and 12H, Fig. 6). The thickness of unit GH2 is greatest (~1 m) at the southern end of the trench, where the meltout till extends to the modern ground surface.

Unit GH3 consists of unconsolidated diamict, which we interpret as a scarp-derived colluvium. At 12H, it flanks the south limb of an anticline where it is an ~1 m thick wedge that pinches out toward the south and unconformably overlies the meltout till (unit GH2). The scarp-derived colluvium is supported by a sandy matrix and contains subrounded-to-rounded pebbles and occasional cobbles and boulders that are more frequent near its basal contact.

Unit GH4 has a matrix that consists of sandy loam and is clast supported. The clasts consist of abundant angular boulders, cobbles, and relatively few pebbles that have varied lithologies, including basalt, intrusive rocks, and schist. South of 12H, the unit is largely overprinted by a <30 cm thick O and Ae soil horizon that is heavily bioturbated and unconsolidated. We designate unit GH4a where, from 3H to 12H, it conformably overlies meltout till (unit GH2) and scarp-derived colluvium (unit GH3). North of 14H, we designate unit GH4b, where this unit overlies lodgment till (unit GH1) above an erosional unconformity. At this location, it thickens to ~0.6 m toward the north. We interpret unit GH4 to be hillslope-derived colluvium developed on the underlying glacial till facies. South of 12H, we interpret that overland flow stripped clay and silt from the matrix of unit GH4a concentrating coarse clasts.

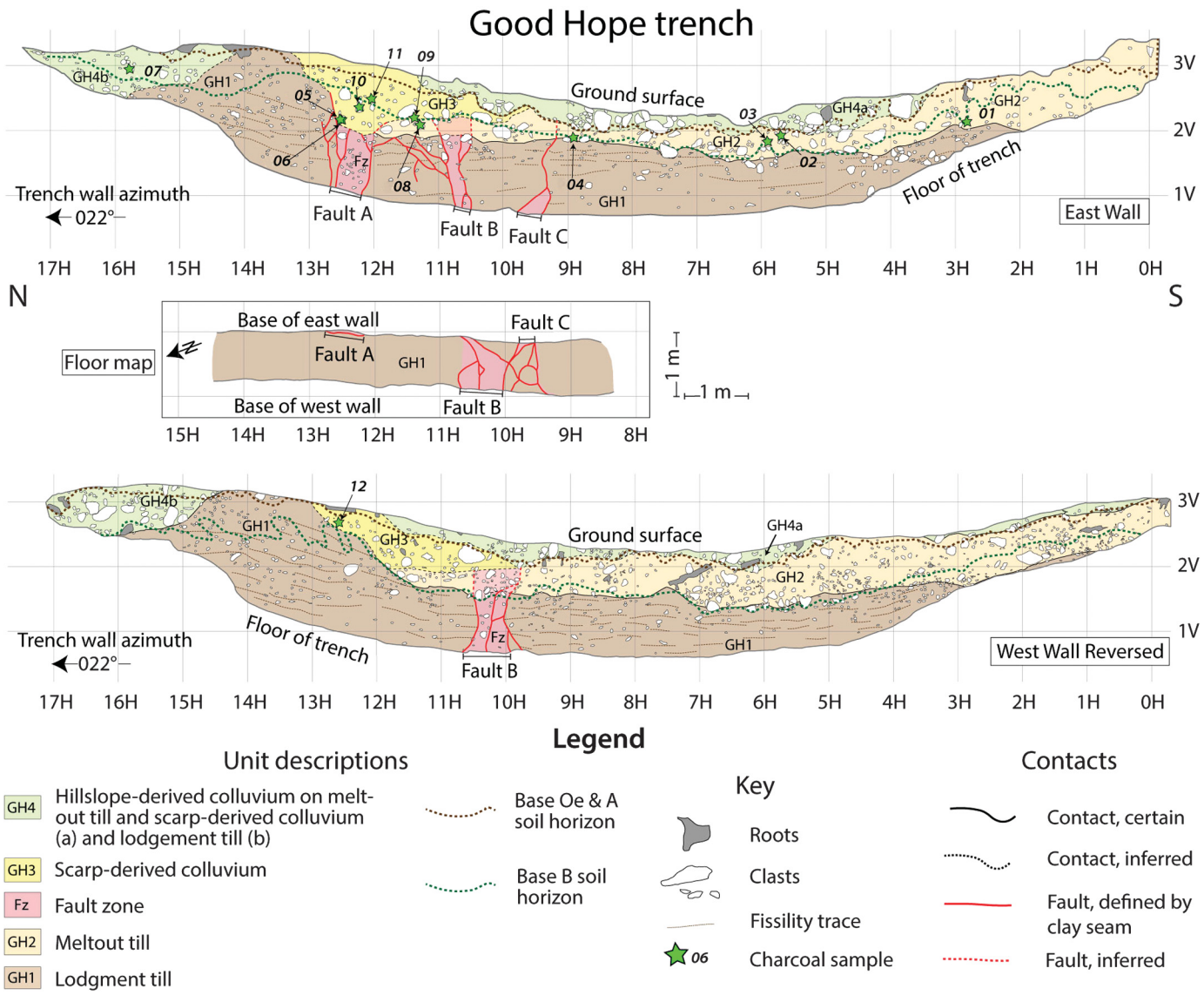

Figure 6. Trench logs for the Good Hope trench. The west wall has been reversed to show correlation with the floor (map view) and east wall. Folding (as seen by warped lodgment till fabric or fissility) and northside up motion on fault A produced a scarp that deposited colluvium on top of lodgment and meltout till. 1 m grid spacing.

The modern O and Ae soil horizon is developed into all four stratigraphic units, and we also map an ~0.5–1 m thick, rust-colored B soil horizon beneath the O and Ae horizons (Fig. 6). Light-gray clay accumulation (C horizon) at the base of the B horizon loosely corresponds with the top of the less-permeable lodgment till (unit GH1) along the length of most of the trench, except where the lodgment till (unit GH1) is topographically higher and eroded due to folding and faulting between 12H and 15H. Here, the base of the B horizon is highly irregular and is ~0.15–0.6 m below the O and Ae horizons.

Faults and folds. Three steeply dipping anastamosing fault zones deform the lodgment till (unit GH1) and the meltout till (unit GH2). Fault A, an ~0.5–0.7 m wide subvertical fault zone that strikes ~130°–150° is only exposed in the east wall of the trench between 12H and 13H and terminates to the west against a 1 cm wide, northeast–southwest-striking subvertical fault exposed in the trench floor (Fig. 6). The lodgment till (unit GH1)–meltout till (unit GH2) contact shows at least 0.5 m of apparent northside up vertical separation across fault A. Where the fault zone crosscuts lodgment till (unit GH2), the matrix is less consolidated, lacks horizontal fissility, and the clasts are randomly oriented. The randomly oriented clasts, less consolidated matrix, and the overlapping wedge of scarp-derived colluvium (unit GH3), which is deposited into the top of this fault zone, indicates material collapse into the fault zone that we interpret as filling of a fissure either during rupture or shortly thereafter.

Fault B is ~0.2–0.5 m wide and is exposed in both trench walls and the trench floor between 10H and 11H

TABLE 1
Descriptions of Stratigraphic Units in the Good Hope Trench

Unit	Interpretation	Lithology	%C/M*	Support	Matrix Texture	%B/C/P†	Clast Angularity	Sedimentary Structures	Munsell Color	Soil Structure
GH1	Lodgment till	Well consolidated silt, sand, clay, pebble, and cobble diamict	20/80	Matrix	Silty clay	1/5/94	Rounded to subrounded	Fissile fabric developed in matrix. Long axes of clasts parallel with glacial flow direction. Discontinuous stratification	Main color: 5 yr 4/2 Mottle: 5 yr 5/1 Stain: 10 yr 4/6 Weathered 5 yr 5/3	Clay film accumulation at top of unit where there is a 5–20 cm thick C horizon; Where unit is nearer to surface B, and C horizon developed throughout unit; Bioturbation of fissile fabric leads to deformation of fabric
GH2	Meltout till	Sand, silt, pebble, cobble, and boulder diamict	60/40	Clast	Sand to silt	10/30/60	Subangular to subrounded	Bioturbation	Bioturbated soil: 2.5 yr 3/4. Less developed soil: 2.5 yr 4/2	Ae horizon through B horizon developed throughout
GH3	Colluvium derived from fault and fold scarp	Sand, pebble, cobble, and boulder diamict	50/50	Matrix	Sand	10/10/80	Subrounded to rounded	Bioturbation	10 yr 5/4	Ae and B horizons developed throughout unit
GH4a, GH4b	Hillslope-derived colluvium	Sand, boulder, cobble, and pebble diamict	65/35	Clast	Sandy loam, sand, silt	50/35/15	Angular to subrounded	Bioturbation	Leached: 5 yr 6/1 Nonleached: 10 yr 4/2	Much of the unit coincides with O/Ae horizon south of 12H

*%C/M = %Clast/%Matrix.
†%B/C/P = %Boulders/%Cobbles/%Pebbles of clasts.

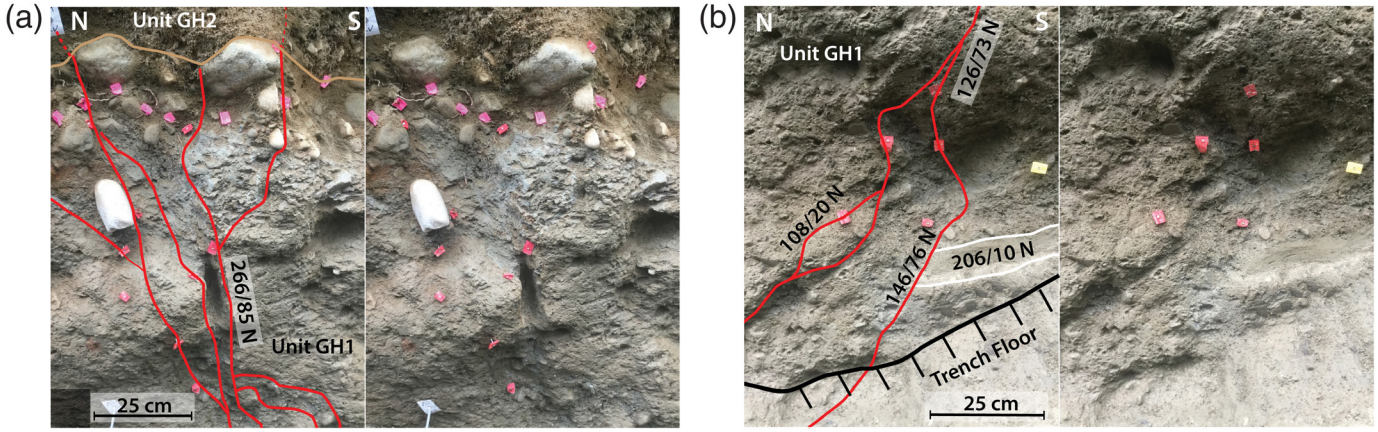

Figure 7. (a) Interpreted (left) and uninterpreted (right) photos showing fault B (solid red lines represent clay seams in fault) in the Good Hope trench at 10.5H, 1V on the east wall. The contact between lodgment till (unit GH1) and meltout till is shown with light-brown solid line. (b) Interpreted (left) and uninterpreted (right) photos showing fine-grained sand bed (solid white) in the lodgment till (unit GH1) truncated by fault C in the east wall of the Good Hope trench at 9.5H, 0V.

(Figs. 6 and 7a). Several small, ~1 cm wide, subvertical anastamosing clay seams located within this fault zone emanate from the fault into the surrounding lodgment till (unit GH1). The clay seams exhibit a lighter-gray color than the surrounding silty clay and contain thin (<5 mm) margins of rust-colored, oxidized till. The fault zone is less discrete where it crosscuts the overlying meltout till (unit GH2), but it can be identified in unit GH2, in the west wall, by vertically rotated cobbles (Fig. 6). Although this fault propagates through the lodgment–meltout till contact, there is no visible offset of this contact, which rules out significant vertical slip on this fault strand given the orientation of the trench near-perpendicular to the fault zone.

Fault C is located south of fault B on the east wall of the Good Hope trench (between 9H and 10H, Figs. 6 and 7b). This fault coalesces with fault B in the trench floor and therefore is not visible in the west wall. Fault C is an ~2–25 cm wide fault zone that, similar to fault B, does not vertically offset the lodgment till (unit GH1)—meltout till (unit GH2) contact; however, it does truncate an ~3 cm thick sand bed observed within the lodgment till (unit GH1), which is not observed north of the fault (Fig. 7b).

The only fault with measurable offset was fault A and we estimate its minimum apparent dip-slip offset by measuring the minimum vertical offset of the lodgment till (unit GH1)—meltout till (unit GH2) contact along a subvertical projection of the fault. On the downthrown block, this contact is mapped continuously to the southern edge of fault A. On the upthrown block, this contact is not visible because it has likely been eroded. However, we assume it is parallel to both the ground surface and the lodgment till fabric and we estimate that its minimum possible elevation is coincident with the ground surface (Fig. 8a). From this inference, we estimate a minimum ~1.1 m of apparent dip-slip offset across fault A after the deposition of unit GH2. Unfortunately we did not find any slickenlines on fault surfaces in the Good Hope trench that would help place additional constraints on fault kinematics.

In addition to faulting, both the fabric defined by the fissility and the upper contact of unit GH1 are folded into a gentle anticline in both walls of the Good Hope trench (between 12H and 15H, Fig. 6). The upper contact of unit GH1 defines a tighter fold than the fissility, which we interpret to be due to vertical offset on fault A and erosion of the topographic scarp.

Clast orientations. We measured 125 lineations of prolate lodgment till (unit GH1) clasts and 105 a/b planes of oblate meltout till (unit GH2) clasts to delineate the presence of sheared Quaternary sediment in the Good Hope trench (Fig. 9). Lodgement till clast measurements from within faults B and C were grouped together, because fault C alone did not contain enough measurable clasts and fault C coalesces with fault B in the trench floor (Fig. 6). Probability tests for a uniform distribution of biaxial azimuths (Bingham test) and the probabilities that the sets of measurements belong to equal distributions (nonparametric Mardia–Watson–Wheeler test) are shown in Table 2. The significance level for each of these tests is $p = 0.05$.

The 50 prolate clasts measured in the undeformed lodgment till (Table A2) in the Good Hope trench exhibit preferred orientations, with gentle-to-moderate plunges and trends subparallel to the dominant glacial flow direction (194.8° ± 2.5°, Fig. 9a), determined from 41 measurements of glacier flow indicators (Table A1) in lidar-derived hillshade and slope maps (Fig. 5). The prolate till clast trends from this data set exhibit a nonuniform distribution, with an average orientation of 38.8° ± 19.2° (Table 2). When considered as a biaxial azimuth, this average orientation is subparallel with the average dominant glacial flow direction associated with the last regional glaciation.

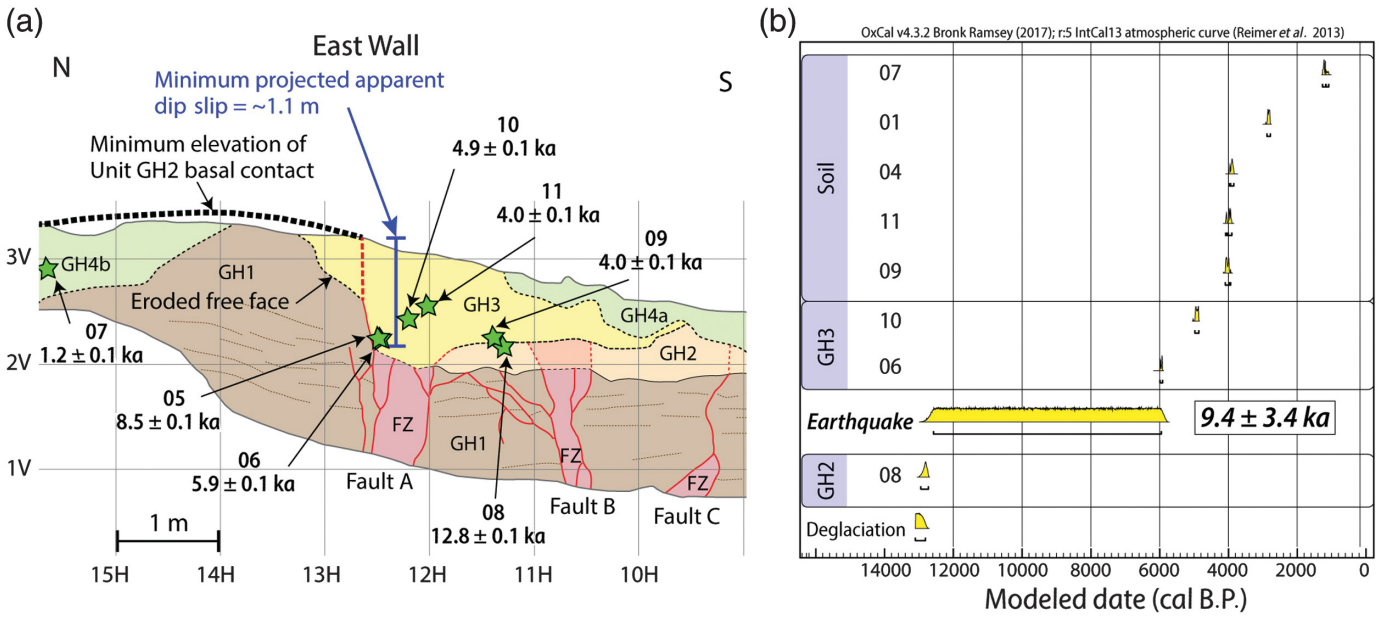

Figure 8. (a) Minimum apparent dip slip on fault A in the east wall of the Good Hope trench and locations of the charcoal samples used in our OxCal model. A minimum of ~1.1 m of dip slip on fault A is calculated by projecting the minimum height of the upthrown unit GH1/unit GH2 contact to the projection of the main slip surface. Calibrated radiocarbon age ranges of macroscopic charcoal samples that define the timing of surface rupture in the Good Hope trench are also shown. Uncertainties are based on 95% confidence interval of probability density functions (PDFs). Legend is the same as Figure 6. (b) OxCal model (Bronk Ramsey, 2017) showing chronological order of the modeled ages (shown as PDFs) of stratigraphy and the surface rupturing earthquake observed in the Good Hope trench. Solid line below shows the 95% confidence intervals of the PDFs. The model inputs are radiocarbon ages shown in Table 3 and the minimum age of deglaciation (~13, 100 cal B.P., Alley and Chatwin, 1979). Further details of the model are shown in Table 4.

Measurements of 50 clast orientations from sheared lodgment till (unit GH1) in faults C and B (Table A3) are approximately perpendicular to the dominant glacial flow direction—an observation that suggests that these clasts may have been rotated during coseismic rupture (Fig. 9a). The clast orientations in faults B and C exhibit a nonuniform distribution, with an average trend of 289.1° ± 23.3° (Table 2) and a moderate-to-gentle plunge. This average trend is oriented approximately perpendicular to the dominant glacial flow direction of 194.8° ± 2.5° and subparallel to the west-northwest strike of the Leech River fault within the vicinity of the Good Hope trench. The biaxial azimuths in undeformed lodgment till, and faults B and C, belong to different populations in which $p(\text{same}) = 1.185 \times 10^{-2}$ (Table 2).

Unlike faults B and C, long-axis clast orientations in fault A (Table A4) exhibit a uniform distribution, and their azimuths do not belong to statistically different populations than clast azimuths in the undeformed till or in faults B and C (Fig. 9a). The orientations of clasts in fault A exhibit steep-to-gentle plunges and a high probability for a uniform, random distribution of trends in which $p(\text{uniform}) = 0.6531$ (Table 2). Because the prolate clasts in fault A exhibit random orientations, they do not correspond with glacial flow direction or fault zone orientations.

A Bingham test suggests the poles to a/b planes of oblate clasts in undeformed meltout till (unit GH2) (Table A5) belong to a statistically different population than the poles to planes in sheared meltout till in fault B (Table A6). Poles to a/b planes in the undeformed meltout till have a $p(\text{uniform}) = 1.682 \times 10^{-6}$ and cluster about a mean plane orientation of 010°/23° (Fig. 9b). The fact that they do not belong to a random distribution but cluster around a mean vector suggests that the meltout till may be imbricated. Imbricated meltout till clasts tend to lie in the plane of deposition and preserve englacial debris fabrics, which vary depending on their location within the glacier (e.g., Boulton, 1971). Therefore, we cannot infer flow direction from the dip direction of the till clasts. In contrast to the undeformed meltout till clasts, the poles to orientations measured in faulted meltout till (fault B) have a $p(\text{uniform}) = 0.3462$, therefore, they may belong to a uniform distribution of points in a sphere. This distribution suggests that the a/b planes of clasts within fault B are not imbricated and have been deformed by fault offset subsequent to their deposition.

Radiocarbon dating. Median calibrated radiocarbon ages from the Good Hope trench (Figs. 6 and 8a) range from 12.8 to 0.2 ka (Table 3). Three samples, 02, 03, and 12, exhibit young ages (185 ± 170 cal B.P., 512 ± 16 cal B.P., and 854 ± 88 cal B.P., respectively). These samples were removed from the OxCal model, because they were sampled from within the modern soil horizon and their ages most likely reflect modern soil development and bioturbation. One sample

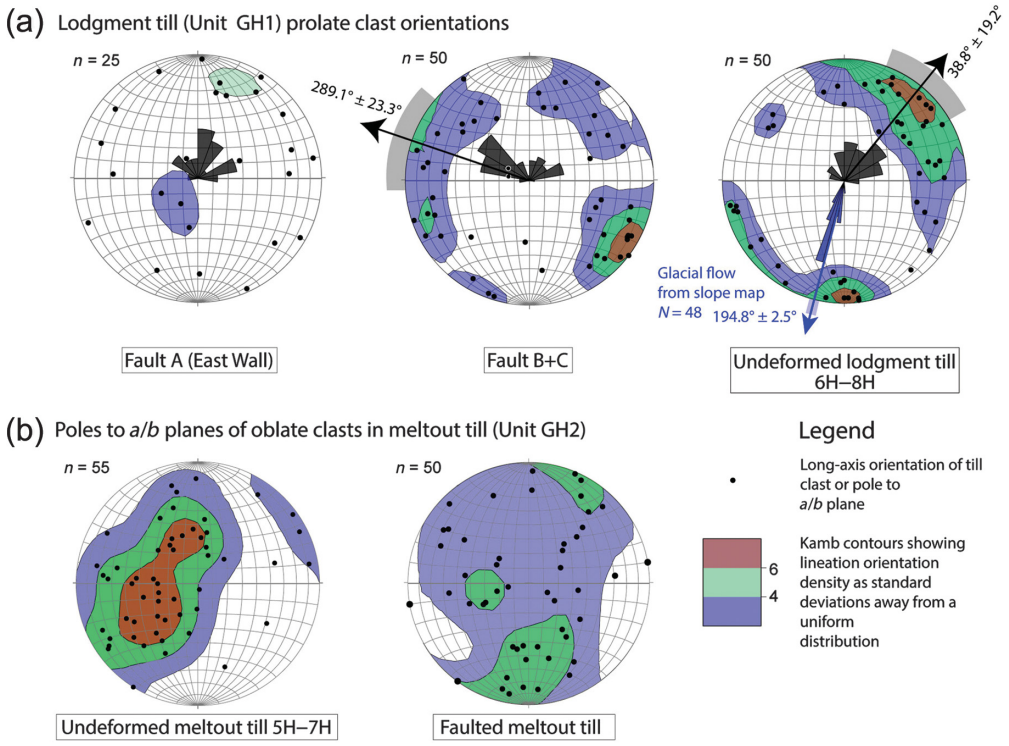

Figure 9. (a) Lower hemisphere equal area stereonet projections showing orientations of the long axes of prolate pebble and cobble clasts in sheared lodgment till from fault A, faults B and C combined, and undeformed lodgment till. Black half-rose diagrams show the distribution of bidirectional azimuths in 20° bins, and arrows show the average bidirectional lineation trend. Uncertainty of the bidirection lineation trend is shown in light gray, beyond the radius of stereonet. Blue half-rose diagram shows distribution of glacial flow directions measured from slope and hillshade maps in 5° bins and the average trend. Uncertainty of the average glacial flow trend is shown in light blue, beyond the radius of stereonet. Radius of the stereonet is equal to 50 data points for rose diagrams. (b) Lower hemisphere equal area stereonet projections of poles to *a*/*b* plane orientations of clasts within undeformed and faulted meltout till (unit GH2) in the Good Hope trench. Undeformed meltout till clasts were measured between 5H and 7H in both east and west walls. These poles fit a mean plane orientation of 010°/23°. Faulted meltout till clast orientations were taken from fault B between 10H and 11H, in both the east and west walls (see Fig. 6). Kamb contours (colored regions) show number of standard deviations away an area (5% of stereonet) is from having a uniform distribution of *n* points. Orientations analyzed using Stereonet 10 (Cardozo and Allmendinger, 2013). For complete list of clast and glacial flow orientations, see Tables A1–A6.

(07) from the meltout till (unit GH2) yields an age of 12.8 ± 0.1 ka, whereas samples from the overlying scarp colluvium (unit GH3) exhibit ages that range from 8.5 to 4.9 ± 0.1 ka. The four remaining charcoal ages were extracted from the B soil horizon developed on the meltout till (unit GH2), the scarp-derived colluvium (unit GH3), and the hillslope-derived colluvium (unit GH4), and range in age from 4.0 to 1.2 ± 0.1 ka. Thus, all of these ages suggest that these samples are in stratigraphic order, with little to no recycling of older charcoal into younger units. The one exception is sample 05 from the scarp-derived colluvium (unit GH3), which yielded an age of 8.5 ± 0.1 ka. This sample is in close proximity to and above sample 06, which yielded a younger age of 5.9 ± 0.1 ka. Considering the proximity of these samples to one another, we consider it likely that sample 05 could be recycled or inherited from an older unit. To consider this possibility, we performed two different OxCal models—one with and one without sample 05—to determine the ages of the stratigraphic units in the Good Hope trench. OxCal codes and tabulated results for both models are provided in the supplemental material.

The age ranges of the scarp-derived colluvium (unit GH3) and the meltout till (unit GH2) determined in our OxCal models bracket the timing of the surface rupturing earthquake that created a topographical scarp. As only one colluvial wedge is exposed in the Good Hope trench (unit GH3), only one surface rupture age is constrained. In the first model, including sample 05, the earthquake rupture event age is 10.7 ± 2.1 ka. In the second model (Table 4; Fig. 8b), without

TABLE 2
Lodgment Clast Orientation Statistics

Sample Set	*p* (Uniform)*	Mean Biaxial Azimuth†	*p* (same) as Fault A‡	*p* (same) as Fault B + C3
Undeformed till	4.06×10^{-8}	38.8° ± 19.2°	0.785	1.185×10^{-2}
Fault A	0.6531	N/A		9.586×10^{-2}
Fault B + C	4.964×10^{-3}	289.1° ± 23.3°		

*Probability that the sample set belongs to a population with a uniform distribution (*p* (uniform)) determined using a Bingham test.
†Mean trend calculated from biaxial azimuths. Only a single azimuth is reported, but azimuth +180° is equally viable.
‡Probability that biaxial azimuths within two sample sets belong to the same distribution determined using a Mardia–Watson–Wheeler test.

TABLE 3
Summary Statistics of Uncalibrated and Calibrated Unmodeled Radiocarbon Concentrations and Ages from the Good Hope Trench

Sample*	Location†	Fraction (modern)	$D^{14}C$ (‰)	^{14}C Age (B.P.)	Maximum Age (cal B.P.)‡	Minimum Age (cal B.P.)	Mean Age (cal B.P.)	Median Age (cal B.P.)	Standard Deviation (cal B.P.)
01	2.85H, 2.08V	0.7107 ± 0.0017	−289.3 ± 1.7	2,745 ± 20	2,876	2,780	2,828	2,826	28
02	*5.75H, 1.94V*	0.9802 ± 0.0022	−19.8 ± 2.2	160 ± 20	*285*	–	*161*	*185*	*85*
03	*5.95H, 1.83V*	0.9443 ± 0.0022	−55.7 ± 2.2	460 ± 20	*529*	*498*	*512*	*512*	*8*
04	8.94H, 1.90V	0.6393 ± 0.0013	−360.7 ± 1.3	3,595 ± 20	3,970	3,841	3,901	3,897	33
05	*12.58H, 2.40V*	0.3831 ± 0.0010	−616.9 ± 1.0	7,710 ± 25	*8,546*	*8,426*	*8,489*	*8,490*	*34*
06	12.55H, 2.21V	0.5241 ± 0.0011	−475.9 ± 1.1	5,190 ± 20	5,990	5,912	5,947	5,939	24
07	15.76H, 2.89V	0.8569 ± 0.0017	−143.1 ± 1.7	1,240 ± 20	1,264	1,081	1,192	1,210	49
08	11.30H, 2.13V	0.2546 ± 0.0009	−745.4 ± 0.9	10,990 ± 30	12,971	12,733	12,840	12,831	62
09	11.40H, 2.13V	0.6323 ± 0.0014	−367.7 ± 1.4	3,685 ± 20	4,088	3,933	4,029	4,036	39
10	12.25H, 2.42V	0.5813 ± 0.0013	−418.7 ± 1.3	4,360 ± 20	4,971	4,860	4,918	4,918	36
11	12.05H, 2.42V	0.6343 ± 0.0014	−365.7 ± 1.4	3,655 ± 20	4,081	3,901	3,983	3,973	51
12§	*12.57H, 2.65V*	0.8935 ± 0.0019	−106.5 ± 1.9	905 ± 20	*911*	*762*	*843*	*854*	*44*

*Samples excluded from favored OxCal model are in italics.
†Macroscopic charcoal samples collected from the east wall of the Good Hope trench.
‡Ages were calibrated using OxCal version 4.3.2 (Bronk Ramsey, 2017) with the IntCal13 atmosphere curve (Reimer *et al.*, 2013). Calibrated age (cal B.P.).
§Sample from west wall.

sample 05, the rupture age is 9.4 ± 3.4 ka. We favor the second model, in which all of the charcoal samples are in stratigraphic order, even though it results in a larger uncertainty (Fig. 8b).

Hummingbird trench

The Hummingbird trench, located 625 m west–northwest of the Good Hope trench (Fig. 5), revealed a stratigraphic sequence we interpret as, starting from the base: basalt (unit HBB), lodgment till (unit HB1), meltout till (unit HB2), and hillslope-derived colluvium (unit HB3) (Fig. 10; Table S3). The Quaternary glacial and postglacial stratigraphy exposed in the Hummingbird trench is similar in composition to that exposed in the Good Hope trench (see supplemental material); however, we did not observe fault offset of glacial and postglacial sediments. Instead, we document brittle faulting of the underlying basalt that we interpret to be related to distinctive bedrock topography.

From 0H to 35H (Fig. 10), the excavation depth of the Hummingbird trench was restricted due to resistant basalt bedrock (unit HBB). The contact between bedrock and overlying deposits is irregular and exhibits ∼0.5–3 m deep and ∼1–10 m wide troughs separated by ridges that are 0.3–1.5 m below ground surface. The linear axes of the ridges and troughs are oriented ∼290°—an orientation that is similar to the ∼3 m high bedrock fault scarp located 20 m west of the trench.

Variably deformed, chlorite and epidote altered, fine-grained basalt overprinted by brittle faulting was observed in the trench floor. From 19H to 27.5H (Fig. 10), we observed well-foliated basalt with 3–10 mm layers of fine-grained epidote and quartz juxtaposed with layers of fine-grained chlorite and mafic minerals. The foliation is subvertical and oriented ∼290°, parallel with the ridges and troughs formed by unit HBB and the bedrock scarp to the west of the trench. This foliation is overprinted by brittle fractures. South of 19H and north of 27.5H, the basalt is massive, fine-grained, and has a mottled texture due to epidote and chlorite alteration. The massive basalt has 10–20 cm spaced <1 cm wide subvertical quartz veins oriented ∼290°. Brittle fractures and faults that overprint the basalt are concentrated within the troughs formed by the bedrock topography and Quaternary sediment in these troughs contains angular basalt boulder- and cobble-sized rip-up clasts. Slickenside orientations and kinematic indicators of faults in the basalt reveal several modes of slip on predominantly west-northwest-striking and moderately to steeply north-dipping faults (Fig. 10). Kinematic inversion of these orientations reveals no consistent slip direction.

We propose that the plucking of rock from brittle fault zones by overriding glaciers, similar to the formation of a roche moutoneé (e.g., Carol, 1947; Lewis, 1954), formed the troughs seen in the bedrock topography and the bedrock scarp ∼20 m east of the trench. Two observations from the Hummingbird trench support this interpretation: the location of the majority of the brittle fractures and faults in bedrock at the base of the bedrock troughs, and the occurrence of angular basalt clasts above the basalt-till contact within these troughs. Our observation that the bedrock scarp to the west of the Hummingbird trench and the ridges and troughs formed by the basalt (unit HBB)–meltout till (unit HB2) contact are parallel with basalt foliation, suggests that brittle faulting may be taking advantage of and aligning parallel with preexisting planes of weakness in the bedrock. This process of bedrock scarp formation may be common in glaciated regions and should be taken into consideration when mapping active faults based on topographic scarps.

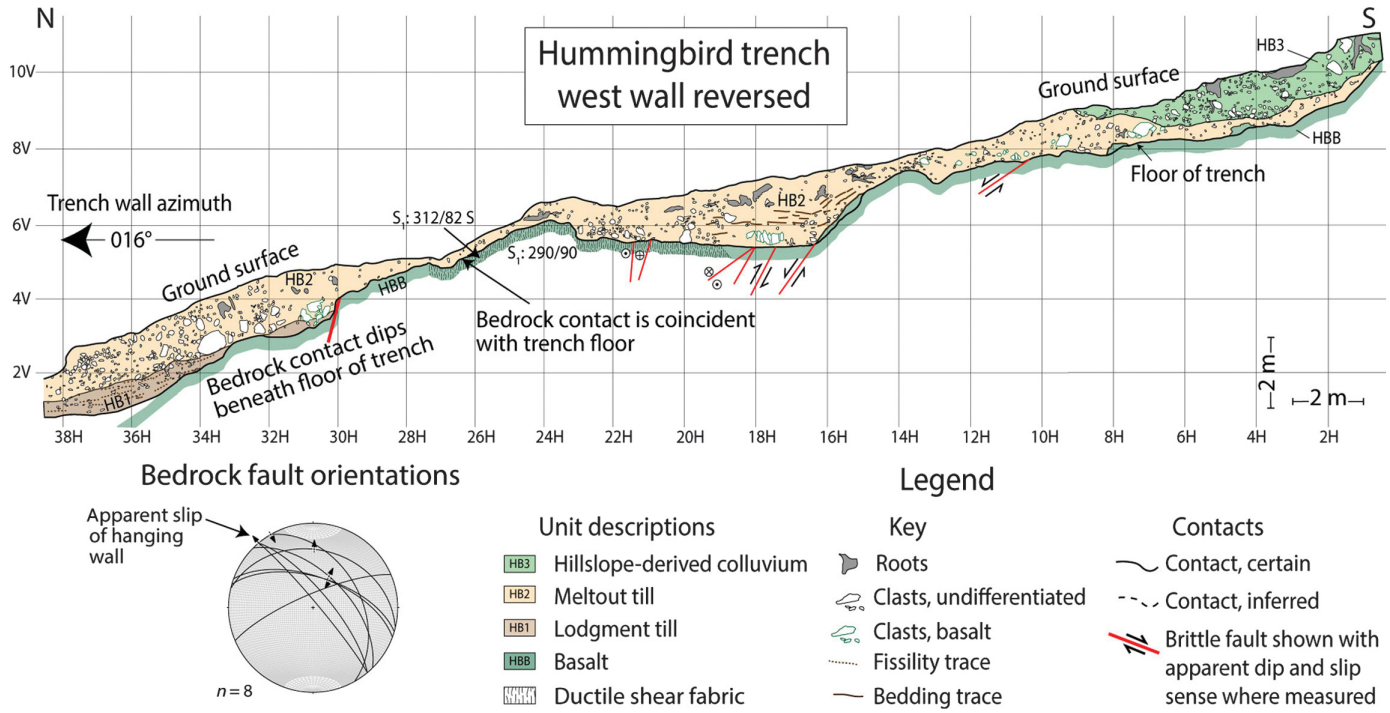

Figure 10. Trench log of the west wall of the Hummingbird trench. It has been reversed to be consistent with the Good Hope trench logs and bedrock geology is shown where it was exposed on the trench floor. Bedrock topographical lows and ridges may be formed by plucking of loose brittle fault zone rock during glaciation. Lower hemisphere stereonet projection shows fault planes and slickenline lineations (black dots) with slip sense (arrows) of the hanging wall relative to the foot wall where they were measured. Apparent slip sense (hanging wall with respect to footwall) was determined from visible offset along faults. Fault plane and slickenline data plotted and analyzed using FaultKin 7.5 (Allmendinger, 2016).

DISCUSSION

Our new geomorphic mapping and paleoseismic trenching reveal evidence for Holocene-active, oblique right-lateral faulting on the Leech River fault, with one surface rupturing earthquake that occurred at 9.4 ± 3.4 ka. We interpret this deformation to be a result of ongoing permanent tectonic strain accumulation and unrelated to (post)glacial stress changes. Therefore, we address how our results affect seismic hazard assessment on southern Vancouver Island and consider

TABLE 4
Summary Statistics of Calibrated Radiocarbon Ages (cal B.P.) from Preferred OxCal Model of the Good Hope Trench Stratigraphy

Name*	Maximum Age (cal B.P.)	Minimum Age (cal B.P.)	Confidence Interval (%)	Mean Age (cal B.P.)	Standard Deviation (cal B.P.)	Median Age (cal B.P.)
07	1,264	1,082	95.4	1,192	49	1210
01	2,876	2,780	95.4	2,828	28	2827
04	3,970	3,841	95.4	3,901	33	3897
11	4,080	3,901	95.4	3,983	51	3973
09	4,089	3,933	95.4	4,029	39	4036
Soil						
10	4,971	4,860	95.4	4,918	36	4918
06	5,990	5,912	95.4	5,947	23	5939
GH3						
Earthquake	12,756	5,984	95.4	9,386	1986	9383
08	12,945	12,725	95.4	12,826	57	12,818
GH2						
Deglaciation	13,103	12,812	95.4	12,963	86	12,970
Ice free†						13,100

*Ages are in stratigraphic order, and were modeled and calibrated using OxCal version 4.3.2 (Bronk Ramsey, 2017) with the IntCal13 atmosphere curve (Reimer *et al.*, 2013).
†Ice free at 13,100 B.P. (Alley and Chatwin, 1979) is used as maximum age for the model.

their consistency with the two proposed models for deformation of the northern Cascadia forearc (Fig. 2).

Fault kinematics

Good Hope trench. A single surface rupturing earthquake deforming both the lodgment till (unit GH1) and the meltout till (unit GH2) best explains our observations of the Quaternary stratigraphy exposed in the Good Hope trench (Fig. 6). Vertical offset of the basal contact of the meltout till (unit GH2) along fault A (Fig. 8) and rotations of meltout till clasts in faults B and C away from their depositional orientation (Fig. 9b) strongly suggest that both till units were deformed. As both units were deformed, we infer that if any postglacial erosion of the lodgment till (unit GH1) occurred, it occurred before the observed surface rupturing earthquake. In addition, as only one scarp-derived colluvial wedge (unit GH3) was observed in the Good Hope trench (Fig. 6), we suggest that faults A, B, and C all ruptured coevally.

We find evidence that both dip slip and strike slip are accommodated by faults in the Good Hope trench. A dip-slip component to faulting is indicated by ~1.1 m of apparent dip slip on fault A (Fig. 8) and folding of lodgment till fissility (Fig. 6). Vertical offset along fault A must have a component of true dip slip and cannot be attributed to only apparent dip slip, because there is vertical separation of the basal contact of the meltout till (unit GH2) in the west wall of the trench and fault A is truncated in the trench floor (Fig. 6). This observation argues that vertical separation observed in the Good Hope trench is mainly due to folding and(or) plastic vertical offset of glacial till above a buried fault (e.g., Brooks *et al.*, 2017) and not a result of apparent lateral offset. The truncation of fault A in the trench floor also shows that it is geometrically improbable for fault A to have enough horizontal offset to have ~1.1 m of apparent vertical offset.

We interpret that the vertical separation measured on the topographic profile (5.2 ± 0.2 m, Figs. 5c and 11b) is related the observed anticline in the Good Hope trench (Fig. 6). As vertical separation in the west wall Good Hope trench is taken up by plastic deformation, we suggest that formation of a broad anticline, with a fold hinge to the north of the Good Hope trench, accounts for the additional ~4 m of vertical offset that is not accounted for by vertical offset along fault A. In addition, erosion of the northern, upthrown block near the fault scarp (e.g., Fig. 11b) would cause an underestimate of vertical offset through near-field observations and may account for some of our observed discrepancy in vertical offset. A similar discrepancy between topographic vertical separation and vertical offset on faults was observed in the Morell *et al.* (2018) trench study, which also may be due to distributed deformation such as folding (e.g., Brooks *et al.*, 2017).

The deformation in the Good Hope trench cannot be explained entirely by dip slip, because there is also significant evidence for strike-slip deformation. The strongest evidence for strike slip on faults B and C is based on the rotation of prolate clasts in sheared lodgment till (unit GH1) and the absence of recognizable vertical displacement on these faults. The ~80° or ~100° rotation about a vertical axis away from mean glacial flow direction of lodgment till (unit GH1) clasts within faults B and C (Fig. 9a) requires shear after deposition. We suggest that postglacial strike-slip shear is the most probable mechanism for this rotation, as we expect that dip slip would induce rotation of the clasts about a horizontal axis (e.g., Cladouhos, 1999). A second line of evidence for strike slip is that fault C truncates a fine-grained sand bed that is observed south of the fault (Fig. 6: east wall, 9.4H, 0.8V; Fig. 7b), but no correlative sand bed is observed in the ~1 m high exposure of this lodgment till north of the fault. We contend that the simplest explanation for this observation is strike-slip offset of a laterally discontinuous sand layer.

We interpret fault A, in addition to accommodating dip slip, as a tension fracture, or fissure, based on clast orientations within the fault (Fig. 9a), and the location of the fault on an anticline (Fig. 6). The randomly orientated prolate clasts observed within fault A suggest that the lodgment till here has been disrupted, but the magnitude of shear strain along this fault was not large enough for the establishment of a preferred clast orientation. Instead, we interpret that gravitational collapse of material into the fault zone during fissuring caused the observed random clast orientations and relatively poor consolidation of the till within this ~0.5 m wide fault zone. Fault A is truncated in the floor of the Good Hope trench against a northeast-striking subvertical fault (Fig. 6), which likely allowed for fissure formation in fault A (Fig. 11). We interpret this fissure to be a tension fracture similar to those that have been observed on mole tracks or pressure ridges that are common during oblique strike-slip rupture (e.g., Philip and Meghraoui, 1983; Bray *et al.*, 1994; Lin *et al.*, 2004; Rao *et al.*, 2011).

Our observations of both strike-slip and dip-slip postglacial fault rupture at our study location indicates oblique strike-slip faulting, which also is consistent with our observations of an anticline or pressure ridge with tension fractures. Surface ruptures of the 1980 M_w 7.1 El Asnam earthquake (Philip and Meghraoui, 1983), the 2001 M_w 7.8 Kunlun earthquake (Lin *et al.*, 2004), the 2010 M_w 6.8 Yushu earthquake (Lin *et al.*, 2011; Rao *et al.*, 2011), and the 2010 M_w 7.1 Darfield earthquake (Quigley *et al.*, 2012), all exhibit pressure ridges and mole tracks with tension fractures occurring on the uplifted and folded ground surface. These fractures tend to occur as en échelon fractures oblique to the main fault strike and are located near the hinge of the pressure ridge (e.g., Philip and Meghraoui, 1983; Lin *et al.*, 2004; Quigley *et al.*, 2012), similar to how fault A is located and oriented in the Good Hope trench (Fig. 11).

The orientation of fault A and our interpretation that it accommodates opening mode fracturing and dip slip is most consistent with right-lateral strike slip on faults B and C

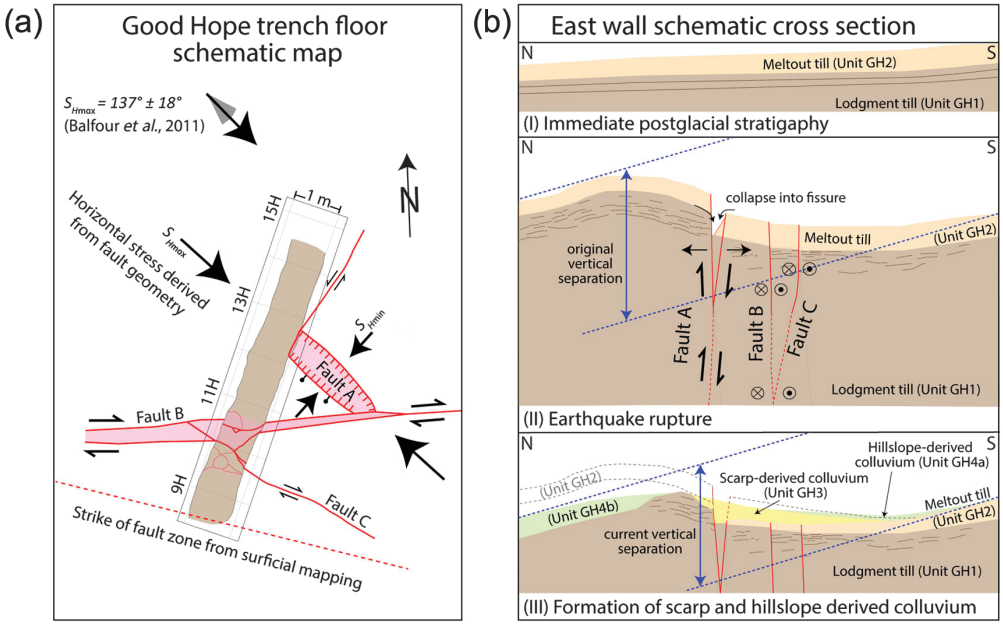

Figure 11. (a) Kinematic interpretation projected onto the Good Hope trench floor depicting concurrent fissure opening on fault A and right-lateral slip on faults B and C. Both the horizontal stress directions determined from fault geometry ($S_{H\,\mathrm{min}}$ is perpendicular to opening mode fault A), and $S_{H\,\mathrm{max}} = 137° \pm 18°$ calculated from seismicity (Balfour *et al.*, 2011) predict right-lateral slip on faults B and C. Seismicity-derived $S_{H\,\mathrm{max}}$ uncertainty shown in gray. (b) Schematic east-facing cross section depicting time series of events that formed the stratigraphy observed in the Good Hope trench. (I) Prerupture glacial stratigraphy. (II) Pressure ridge and tension crack formation and dip slip on fault A and strike-slip faulting on faults B and C during earthquake rupture. (III) Formation of scarp-derived and hillslope-derived colluvium. Approximate vertical separation of the ground surface immediately after fault rupture (II) and at present (III) are denoted with dashed blue lines and illustrate the discrepancy between minimum vertical offset on fault A and vertical offset of the ground surface. Locations of faults at depth in (II) are uncertain and denoted with dashed red lines. Legend is same as Figure 6.

(Fig. 11a). Two lines of evidence support this interpretation of right-lateral slip. First, the predicted orientation of $S_{H\,\mathrm{max}}$, based on the orientation of the opening mode fissure (fault A) at the Good Hope trench predicts right-lateral slip on faults B and C (Fig 11a). Opening mode tension fractures in brittle strike-slip fault systems are often aligned perpendicular to $S_{H\,\mathrm{min}}$ and parallel with $S_{H\,\mathrm{max}}$ (e.g., Bartlett *et al.*, 1981; Sanderson and Marchini, 1984; Fossen, 2016), and this relation has been recognized in surface ruptures (Lin and Nishikawa, 2011; Rao *et al.*, 2011; Quigley *et al.*, 2012). Second, our fault geometry-derived $S_{H\,\mathrm{max}}$ orientation is also parallel with $S_{H\,\mathrm{max}} = 137° \pm 18°$, independently calculated from seismicity (Fig. 11a, Balfour *et al.*, 2011). Right-lateral slip would still be predicted on these faults if an approximately north-northwest–south-southeast regional $S_{H\,\mathrm{max}}$ orientation (Fig. 1c) is considered, even though fault A would be less favorably oriented as a tension crack.

High rates of erosion and potential strike-slip offset, comparable to the 2 m resolution of the lidar DEM used for geomorphic mapping, explain why we do not observe right-lateral offset of geomorphic features at our study site. Crustal surface rupturing strike-slip earthquakes, with comparable vertical surface offsets to the minimum vertical offset we infer in the Good Hope trench (~1.1 m), include the 1992 M_w 7.3 Landers earthquake in southern California (Zachariasen and Sieh, 1995), the 2010 M_w 7.1 Darfield earthquake in New Zealand (Quigley *et al.*, 2012), and the 2019 M_w 7.1 Ridgecrest earthquake in eastern California (Brandenberg *et al.*, 2019). These earthquakes produced $\lesssim$5 m of horizontal surface offset and could represent the approximate strike-slip offset during a surface rupturing earthquake on the Leech River fault. High-precipitation rates and dense vegetation on southern Vancouver Island results in intense erosion and bioturbation of Quaternary sediment, which have inevitably degraded the fault scarp and could have partially to fully realigned channels and interfluves that were originally offset by ~5 m (e.g., Burbank and Anderson, 2011; Zielke, 2018; Reitman *et al.*, 2019). This degradation and realignment would have reduced and obscured the apparent strike-slip surface offset along the Leech River fault both in lidar-based maps and beneath thick vegetation in the field.

Hummingbird trench. Strike-slip and dip-slip faulting observed in basalt at the base of the Hummingbird trench (Fig. 10), 625 m west–northwest along strike from the Good Hope trench, is typical of brittle strike-slip faulting in bedrock. These strike-slip faults can result in the formation of flower structures or fault duplexes that contain both strike-slip and dip-slip faults (e.g., Wilcox *et al.*, 1981; Woodcock and Fischer, 1986; Sylvester, 1988; Bayasgalan *et al.*, 1999; Woodcock and Rickards, 2003; Toda *et al.*, 2016). Fault slickenline orientations show abrupt meter-scale spatial changes in fault slip sense (Fig. 10), which is also common on strike-slip faults where block rotation can be accommodated on multiple fault strands (e.g., Woodcock and Fischer, 1986; Sylvester, 1988; Woodcock and Rickards, 2003).

Complex surface rupture during strike-slip earthquakes, such as the 2001 Kunlun earthquake (Lin *et al.*, 2004), 2010

Landers earthquake (Aydin and Du, 1995; Zachariasen and Sieh, 1995), and 2016 Kunamoto earthquake (Toda *et al.*, 2016), can explain why fault rupture of Quaternary sediments was observed at the Good Hope trench but not along strike at the Hummingbird trench. First, it is possible that the earthquake rupture observed in the Good Hope trench terminated before reaching the Hummingbird trench. Second, the topographic scarp that the Good Hope trench was excavated across projects west–northwest to the very northern end of the Hummingbird trench (Fig. 5), where a road cut may obscure the active fault scarp. Third, variations in vertical slip along other strike-slip surface ruptures have been observed (e.g., Zachariasen and Sieh, 1995; Quigley *et al.*, 2012; Gold *et al.*, 2013), and a topographical scarp produced by surface rupture near the Hummingbird trench may have been minor (<0.5 m) compared with the scarp at the Good Hope trench. The location of the Good Hope trench at a right-stepping jog of the surface trace of the fault (Fig. 5) implies compression (along a right-lateral fault), generating increased vertical separation and scarp height. If the scarp along strike is subdued in comparison, it may not be visible in bare-Earth lidar images and we speculate that it could be located north or south of the Hummingbird trench. Finally, segmentation of surface ruptures during earthquake surface rupture is common and kilometer-wide gaps can occur along strike or between en échelon fault segments (e.g., Fig. 5a; Zachariasen and Sieh, 1995; Lin and Nishikawa, 2011; Gold *et al.*, 2013). Therefore, it is possible that the Hummingbird trench was excavated in one of these gaps.

Comparison with previous paleoseismic trench results. Our interpretation of right-lateral fault slip at the Good Hope trench and dip-slip surface ruptures observed at the previous trenches on the Leech River fault suggest along-strike variation of kinematics that can be also be explained by complex strike-slip fault behavior. At the previous Leech River fault trench site 7 km west-northwest of this study (i.e., Morell *et al.*, 2018), three surface rupturing north side up dip-slip earthquakes are observed; however, it was not possible to make the distinction between a compressional or extensional fault system. These previous trenches may only record dip slip due to their location on a restraining bend and (or) slip partitioning on strike-slip surface ruptures. These previous trenches are located where a 20° change in orientation of fault strike occurs (Fig. 3), and right-lateral slip would produce a constraining bend and local reverse faulting. In addition, strike-slip surface ruptures can be highly irregular with dip slip and strike slip partitioned on different strands of the fault (e.g., Chen *et al.*, 2001; Weinberger, 2014; Barnhart *et al.* 2015; Toda *et al.*, 2016). If complex fault rupture occurred along this stretch of the Leech River fault, fault kinematics at the Good Hope trench could vary from those observed in the previous trenches 7 km away.

Evaluating (post)glacial stress versus tectonic stress as an origin for deformation in the Good Hope trench

There is evidence in glaciated terranes that earthquakes and surface rupture can be triggered by changes in static stress during and after glaciation. Subglacial fractures (e.g., Muir-Wood, 1989; Boulton and Caban, 1995; Thorson, 2000; Jarman and Ballantyne, 2002), sackungen (e.g., McCalpin and Irvine, 1995; Hippolyte *et al.*, 2006), and surface rupturing earthquakes (e.g., Anderson *et al.*, 1989; Davenport *et al.*, 1989; Muir-Wood, 1989; Lagerbäck, 1990; Jarman and Ballantyne, 2002) have all been attributed to these stress changes. Because the range of the earthquake rupture age in the Good Hope trench (9.4 ± 3.4 ka, Fig. 8b) almost extends back to deglaciation (~13,100 cal B.P., Alley and Chatwin, 1979), we evaluate the possibility that the observed deformation in the Good Hope trench could be related to glacial stresses and find that our observations are not consistent with their defining characteristics.

Our observations are not accordant with faulting and fracturing of subglacial sediment that is a result of stress imparted on the earth's surface beneath thick ice sheets (e.g., Muir-Wood, 1989; Boulton and Caban, 1995; Thorson, 2000; Jarman and Ballantyne, 2002). One potential mechanism for fracture and clay seam development is fracturing and escape of pressurized water from permeable units below the nonpermeable clay and silt (e.g., Boulton and Caban, 1995; Van Der Meer *et al.*, 1999; Evans *et al.*, 2006). These structures are observed to widen downward and contain entrained sediment from more permeable lower units (e.g., Boulton and Caban, 1995; Rijsdijk *et al.*, 1999; Van Der Meer *et al.*, 1999; Evans *et al.*, 2006). However, the sediment we observe within fault zones in the Good Hope trench has the same matrix and clast grain size as the wallrock (although deformed) and is unlikely to be injected from permeable coarser-grained units. Also, the presence of offset on fault A (Fig. 6), the truncation of a sand bed by fault C (Fig. 7), and rotated prolate clasts within faults B and C (Fig. 9) shows that slip is accommodated in these fault zones, and the observed clay seams are not just minor joints and fractures in the lodgment till.

We also rule out the formation of sackungen formed during postglacial isostatic rebound. Sackungen are usually contour- and ridge-parallel linear features that form during deep-seated gravitational slope deformation or during gravitational spreading of bedrock ridges (e.g., McCalpin and Irvine, 1995), and they may be coseismic (e.g., Hippolyte *et al.*, 2006; Delano *et al.*, 2018). Opening mode fracturing on fault A could be a result of deep-seated slope failure; however, the location of the fault near the base of the slope, which is only ~200 m to the north (Fig. 5), makes this unlikely. Strike slip on faults B and C is also unlikely to be a result of any gravitational processes that result in dip-slip faulting (e.g., Bovis, 1982; McCalpin and Irvine, 1995). Finally, sackungen also tend to occur in swarms of multiple parallel scarps (e.g., McCalpin, 1999; Hippolyte *et al.*,

2006), but only one or two parallel scarps are identified along the Leech River fault in our study area (Fig. 5).

Changes in lithostatic stress connected with deglaciation have been shown to trigger earthquakes (e.g., Anderson *et al.*, 1989; Davenport *et al.*, 1989; Muir-Wood, 1989; Lagerbäck, 1990; Jarman and Ballantyne, 2002; Craig *et al.*, 2016), but the principal stress directions and kinematics of earthquake rupture we observe in the Leech River fault trenches argue for a tectonic origin. Postglacial release of vertical stress increases deviatoric stress if σ_3 is vertical and can cause reverse faulting (Muir-Wood, 1989; Jarman and Ballantyne, 2002), which may have resulted in dip slip on fault A in the Good Hope trench and in the Morell *et al.* (2018) trenches. However, postglacial strike-slip faulting on faults B and C and stress inversion (e.g., Balfour *et al.*, 2011) suggest that σ_3, at this location, is horizontal and the deviatoric stress would not be affected by glacial unloading. In addition, if deglaciation was responsible for releasing long-term tectonic strain built up during glaciation, a clustering of rupture events would be expected during postglacial isostatic rebound (e.g., Muir-Wood, 1989; Craig *et al.*, 2016). However, two of the observed earthquake rupture ages at the Morell *et al.* (2018) trenches (1.7 ± 0.1 and 2.2 ± 0.1 ka) occurred well after postglacial isostatic rebound was complete in the middle Holocene (Clague and James, 2002), which suggests that tectonic stresses continue to drive deformation on the Leech River fault.

Hazard implications

The results from our study further establish the presence of Holocene-active forearc faults in the northern Cascadia and help determine the maximum rupture length on the Leech River and the Devils Mountain fault systems. Rupture length is a key criterion in seismic hazard models of northern Cascadia that take into account earthquakes on active crustal faults to calculate hazard that results from ground shaking (Halchuk *et al.*, 2019; Kukovica *et al.*, 2019). A confident correlation of the slip event recorded in the Good Hope trench, with slip events observed in the Morell *et al.* (2018) trenches and on faults along strike of the Leech River fault, is not possible due to the large uncertainty in our event age. However, the combination of these earthquake records reveal that fault rupture on the Leech River fault could possibly propagate along the Devils Mountain fault. Morell *et al.* (2018) recorded three rupture events on the Leech River fault, and only one event, at 8.7 ± 0.3 ka, falls within the age range of our slip event (9.4 ± 3.4 ka). On the Devils Mountain fault, the along-strike extension of the Leech River fault to the east, paleoseismic investigations by Personius *et al.* (2014) record an earthquake at 8.1 ± 0.1 ka that also overlaps with the age range of our event. These potential correlations raise the possibility of synchronous fault rupture of the eastern portion of the Leech River fault with the Devils Mountain fault. An event involving both of these faults could have a rupture length >100 km, and empirical fault scaling relationships (e.g., Wesnousky, 2008; Stirling *et al.*, 2013) show that a strike-slip rupture of this length can result in an $M_w > 7$ earthquake. Earthquake rupture of this magnitude at the Good Hope trench site has the potential to cause strong shaking and damage in the Victoria metropolitan area (10 km to the east) and other population centers in the region (e.g., Bellingham, Port Angeles, Anacortes, Washington).

In addition to the hazard the Leech River fault presents to southern Vancouver Island from ground shaking, coseismic surface rupture could directly damage infrastructure that lies on the fault trace. Calculating the hazard that results from coseismic surface rupture (probabilistic fault displacement hazard analysis, e.g., Coppersmith and Youngs, 2000; Youngs *et al.*, 2003; Petersen *et al.*, 2011) requires a range of data, including the location of active fault ruptures (e.g., Coppersmith and Youngs, 2000). Our mapping of a Holocene coseismic surface rupture at the Good Hope trench is within ~25 km of key infrastructure on southern Vancouver Island, such as the Jordan River hydroelectric dam, and roads, bridges, and various other utilities in the Victoria metropolitan area (Fig. 3). Continuing the mapping of Holocene surface ruptures on the Leech River fault along strike will be important to improve assessments of hazard to infrastructure in this region.

Implications for regional tectonics

Our study is the first to show evidence for postglacial oblique right-lateral surface rupture on the Leech River fault, and our interpretation of a right-lateral fault system with the formation of a pressure ridge implies that the Leech River fault does not accommodate significant north–south shortening. This interpretation argues against a forearc deformation model in which thrust faulting on the Leech River fault accommodates northward migration of the Oregon block against a rigid Canadian backstop (e.g., Fig. 2a; Wells *et al.*, 1998; Wang *et al.*, 2003; Sherrod *et al.*, 2013). Instead, we infer that north–south shortening across the Olympic Mountains predicted by the GNSS velocity field (Fig. 1b) is accommodated by oroclinal bending (Fig. 2b) and reverse faulting and folding to the south and east of and within the Olympic Mountains.

Oblique right-lateral slip on the Leech River fault is consistent with this structure accommodating bending of the Olympic orocline (e.g., Finley *et al.*, 2019) and(or) westward extrusion of the Olympic Mountains (e.g., Nelson *et al.*, 2017). Counterclockwise rotation of northern Cascadia about an orocline with a vertical axis in the Olympic Mountains predicts right-lateral flexural slip on west-northwest-striking faults (e.g., Fig. 2b; Donath and Parker, 1964; Hollingsworth *et al.*, 2006), consistent with our observations and studies on other west-northwest-striking crustal faults north of the Olympic Mountains (Fig. 2; Johnson *et al.*, 1996; Personius *et al.*, 2014; Nelson *et al.*, 2017; Greene *et al.*, 2018; Schermer *et al.*,

2020). Flexural slip would also predict an increase in strike-slip rates or displacement away from the fold hinge of the orocline (e.g., Fossen, 2016), which we cannot verify without strike-slip rates along the Leech River fault. Upper crustal seismicity (Fig. 1c) is diminished along the northwest limb of the orocline and may reflect a reduction in slip; however, reduced forearc seismicity toward the trench has also been hypothesized to be a result of subduction interface permeability (Savard *et al.*, 2018). Our hypothesis that right-lateral slip on the Leech River fault accommodates bending of the Olympic orocline is also consistent with westward extrusion of the Olympic Mountains relative to stable NA (Nelson *et al.*, 2017; Finley *et al.*, 2019). This extrusion may be accommodated by right-lateral west-northwest-striking faults north of the Olympic Mountains, including the Leech River fault and left-lateral west-southwest-striking faults south of the Olympic Mountains (Nelson *et al.*, 2017; Finley *et al.*, 2019). West and northwest directed residual GNSS velocities on the northwest coast of the Olympic Peninsula and southwest coast of Vancouver Island (e.g., Mazzotti *et al.*, 2002, 2011) are consistent with trenchward extrusion. If this model is correct, our observations imply that the forearc crust as far north as the Leech River fault may also be extruding west with respect to stable NA.

The Quaternary oblique right-lateral kinematics that we document on the Leech River fault are opposite (in lateral sense) to left-lateral and thrust faulting that is interpreted during Eocene accretion of the Crescent terrane to ancestral NA (Fairchild and Cowan, 1982; Clowes *et al.*, 1987; England *et al.*, 1997; Johnston and Acton, 2003; Eddy *et al.*, 2017), indicating a possible temporal switch in kinematics. A similar switch in kinematics is also observed on the Devils Mountain fault (Personius *et al.*, 2014). Ongoing right-lateral slip on the Leech River fault may have initiated during bending of the Olympic orocline that commenced ~18 Ma (Wells and McCaffrey, 2013). This temporal switch may also have coincided with the counterclockwise rotation of Leech River fault with respect to the maximum horizontal stress directions. These hypotheses could be tested by determining the timing of the switch in fault kinematics on the Leech River fault.

CONCLUSIONS

Exposure of deformed Quaternary glacial till in the Good Hope trench and brittle faulting in the Hummingbird trench reveals evidence for oblique right-lateral strike-slip fault rupture on the Leech River fault. Surface rupture of the fault does not display characteristics associated with glacially derived deformation and we suggest that the observed deformation is tectonic strain. In the Good Hope trench, oblique right-lateral fault rupture formed an anticline that deformed glacial sediments deposited during and immediately after the last glacial maximum (~13,100 cal B.P., Alley and Chatwin, 1979). Analyses of prolate clast orientations differentiate between sheared and undeformed glacial till and suggest strike-slip faulting coupled with opening mode fracture and fissure filling. The fault geometry observed in the Good Hope trench, paired with previously calculated $S_{H\,\max}$ directions (Balfour *et al.*, 2011), suggest that the Leech River fault is accommodating oblique right-lateral slip that is consistent with observed microseismicity (Li *et al.*, 2018) and slip on the along-strike Devils Mountain fault (Personius *et al.*, 2014; Barrie and Greene, 2018) and southern Whidbey Island fault (Johnson *et al.*, 1996). Radiocarbon dating of the scarp-derived colluvium and offset meltout till indicates an earthquake rupture age of 9.4 ± 3.4 ka, which overlaps with earthquake events reported along strike on the Leech River fault (Morell *et al.*, 2018) and the Devils Mountain fault (Personius *et al.*, 2014). This overlap emphasizes the possibility for a $\gtrsim$100 km fault rupture along both the Leech River fault and the Devils Mountain fault and the potential for these faults together to host $M_w > 7$ earthquakes based on fault scaling relationships. We suggest that complex strike-slip fault rupture along the Leech River fault explains the lack of observed Holocene faulting at the Hummingbird trench 625 m west-northwest of the Good Hope trench, as well as the recognition of only dip-slip rupture at the paleoseismic trench site 7 km west-northwest of our study (Morell *et al.*, 2017, 2018).

Our study, along with the recognition of primarily oblique right-lateral slip on other west-northwest-striking crustal faults north of the Olympic Mountains (e.g., Johnson *et al.*, 1996; Personius *et al.*, 2014; Nelson *et al.*, 2017; Barrie and Greene, 2018; Schermer *et al.*, 2020), implies that faults in this region do not accommodate large amounts of north–south shortening against a rigid backstop via thrust faulting (e.g., Wells *et al.*, 1998; Wang *et al.*, 2003; Sherrod *et al.*, 2013). Instead, oblique right-lateral slip in this region may accommodate flexural slip and westward extrusion of the Olympic Mountains, as suggested in recent tectonic models that invoke bending of an orocline about a vertical hinge axis in the Olympic Mountains (e.g., Nelson *et al.*, 2017; Finley *et al.*, 2019).

DATA AND RESOURCES

The U.S. Geological Survey (USGS) Quaternary faults and fold database used for Figure 2c is available at https://www.usgs.gov/natural-hazards/earthquake-hazards/faults (last accessed March 2020). The light detection and ranging (lidar) dataset (James *et al.*, 2010) used for our digital elevation models (DEMs) and slope maps of our study area (Fig. 5) is available at https://geoscan.nrcan.gc.ca/starweb/geoscan/servlet.starweb?path=geoscan/fulle.web&search1=R=285486 (last accessed June 2020). The Ø. Hammer Past program version 3.21 (v.3.21) used for statistical analyses of our clast orientation data (Table 2) is available at https://folk.uio.no/ohammer/past/ (last accessed July 2019). The R. Allmendinger Stereonet program v.10.1.6 used for plotting and analyzing glacial flow directions and clast orientations (Fig. 9) is available at http://www.geo.cornell.edu/geology/faculty/RWA/programs/stereonet.html (last accessed September 2018). The C. Bronk Ramsey, OxCal 14C calibration program, v.4.3. is available at https://c14.arch.ox.ac.uk/oxcal.html (last accessed June 2020). The R. Allmendinger FaultKin

7.5 program used for plotting and analyzing fault plane and slickenline data in the Hummingbird trench (Fig. 10) is available at http://www.geo.cornell.edu/geology/faculty/RWA/programs/faultkin.html (last accessed October 2017). The supplemental material provides detailed stratigraphic descriptions of the Hummingbird trench and large-format high-resolution trench logs, interpreted photomosaics, and uninterpreted photomosaics of the Good Hope and Hummingbird trenches. The supplemental material also includes tables of our preferred and alternate OxCal model age results and the OxCal codes for each model.

ACKNOWLEDGMENTS

The authors would like to thank Kapoor Lumber and the Capital Regional District (CRD) for providing land access to our trench sites. Great appreciation is extended to Johanna Fischi, Vic Levson, Alice Telka, Steve Byrne, Matthew Sypus, Elena Savidge, and Fengzhou Tan, who all assisted in our paleoseismic trench study and provided invaluable input to our research. Walter Langer of AllTerra Excavating Ltd. excavated our trenches and without his expertise, this study would not have been possible. The authors also would like to thank the Keck Carbon Cycle AMS laboratory for our radiocarbon analyses. The authors thank Brian Penserini for reading over our article, and the authors are grateful to Y. Klinger, S. Angster, K. Reicherter, and one anonymous reviewer for their thoughtful suggestions and reviews. Funding for this project is provided by National Science Foundation (NSF) EAR Grant Number 1756943 to K. Morell and Grant Number 1756834 to C. Regalla. This work was also supported by a National Science and Engineering Research Council of Canada Postgraduate Doctoral scholarship (NSERC PGS D) to N. Harrichhausen.

Any use of trade, product, or firm names is for descriptive purposes only and does not imply endorsement by the U.S. Government.

REFERENCES

Adams, B. A., and T. A. Ehlers (2017). Deciphering topographic signals of glaciation and rock uplift in an active orogen: A case study from the Olympic Mountains, USA, *Earth Surf. Process. Landf.* **42,** no. 11, 1680–1692.

Alley, N. F., and S. C. Chatwin (1979). Late Pleistocene history and geomorphology, southwestern Vancouver Island, British Columbia, Canadian, *J. Earth Sci.* **16,** no. 9, 1645–1657.

Allmendinger, R. W. (2016). FaultKin 7.5 for Mac OS X Windows and Linux, 31, available at http://www.geo.cornell.edu/geology/faculty/RWA/programs/faultkin.html (last accessed December 2017).

Allmendinger, R. W., and G. González (2010). Invited review paper: Neogene to Quaternary tectonics of the coastal Cordillera, northern Chile, *Tectonophysics* **495,** nos. 1/2, 93–110.

Anderson, W. A., J. T. Kelley, H. W. Borns, and D. F. Belknap (1989). Neotectonic activity in coastal Maine: United States of America, in *Earthquakes at North-Atlantic Passive Margins: Neotectonics and Postglacial Rebound*, S. Gregersen and P. W. Basham (Editors), Springer, Dordretch, the Netherlands, 195–212.

Armstrong, J. E., D. R. Crandell, D. J. Easterbrook, and J. Noble (1965). Late Pleistocene stratigraphy and chronology in southwestern British Columbia and northwestern Washington, *Geol. Soc. Am. Bull.* **76,** no. 3, 321–330.

Aydin, A., and Y. Du (1995). Surface rupture at a fault bend: The 28 June 1992 Landers, California, earthquake, *Bull. Seismol. Soc. Am.* **85,** no. 1, 111–128.

Babaahmadi, A., and G. Rosenbaum (2015). Kinematics of orocline-parallel faults in the Texas and Coffs Harbour oroclines (eastern Australia) and the role of flexural slip during oroclinal bending, *Aust. J. Earth Sci.* **62,** no. 8, 933–948.

Balfour, N. J., J. F. Cassidy, S. E. Dosso, and S. Mazzotti (2011). Mapping crustal stress and strain in southwest British Columbia, *J. Geophys. Res.* **116,** no. B3, doi: 10.1029/2010JB008003.

Barnett, E. A., B. L. Sherrod, J. F. Hughes, H. M. Kelsey, J. L. Czajkowski, T. J. Walsh, T. A. Contreras, E. R. Schermer, and R. J. Carson (2015). Paleoseismic evidence for late Holocene tectonic deformation along the saddle mountain fault zone, southeastern Olympic peninsula, Washington, *Bull. Seismol. Soc. Am.* **105,** no. 1, 38–71.

Barnhart, W. D., R. Briggs, N. G. Reitman, R. D. Gold, and G. Hayes (2015). Evidence for slip partitioning and bimodal slip behavior on a single fault: Surface slip characteristics of the 2013 Mw7. 7 Balochistan, Pakistan earthquake, *Earth Planet. Sci. Lett.* **420,** 1–11.

Barrie, J. V., and H. G. Greene (2018). The Devils Mountain fault zone: An active Cascadia upper plate zone of deformation, Pacific Northwest of North America, *Sediment. Geol.* **364,** 228–241.

Bartlett, W. L., M. Friedman, and J. M. Logan (1981). Experimental folding and faulting of rocks under confining pressure Part IX. Wrench faults in limestone layers, *Tectonophysics* **79,** nos. 3/4, 255–277.

Batschelet, E. (1981). *Circular Statistics in Biology*, Academic Press, New York, New York.

Batt, G. E., M. T. Brandon, K. A. Farley, and M. Roden-Tice (2001). Tectonic synthesis of the Olympic Mountains segment of the Cascadia wedge, using two-dimensional thermal and kinematic modeling of thermochronological ages, *J. Geophys. Res.* **106,** no. B11, 26,731–26,746.

Bayasgalan, A., J. Jackson, J.-F. Ritz, and S. Carretier (1999). Forebergs', flower structures, and the development of large intracontinental strike-slip faults: The Gurvan Bogd fault system in Mongolia, *J. Struct. Geol.* **21,** no. 10, 1285–1302.

Bennett, S. E. K., M. Reid, J. Delano, K. Scharer, H. Kelsey, D. McPhillips, B. Sherrod, A. Streig, H. K. G. Martin, and S. Mahan (2017). Late Quaternary earthquakes on the Canyon River fault, Olympic Mountains, Washington: Linking active faults in the Puget Lowland to offshore Cascadia, *Geological Society of America Abstracts with Programs*, Vol. 49, Seattle, Washington, 24 October 2017.

Bingham, C. (1974). An antipodally symmetric distribution on the sphere, *Ann. Stat.* **2,** no. 6, 1201–1225.

Blakely, R. J., B. L. Sherrod, J. F. Hughes, M. L. Anderson, R. E. Wells, and C. S. Weaver (2009). Saddle Mountain fault deformation zone, Olympic Peninsula, Washington: Western boundary of the Seattle uplift, *Geosphere* **5,** no. 2, 105–125.

Blakely, R. J., B. L. Sherrod, C. S. Weaver, R. E. Wells, A. C. Rohay, E. A. Barnett, and N. E. Knepprath (2011). Connecting the Yakima fold and thrust belt to active faults in the Puget Lowland, Washington, *J. Geophys. Res.* **116,** no. B7, doi: 10.1029/2010JB008091.

Blakely, R. J., R. E. Wells, T. L. Tolan, M. H. Beeson, A. M. Trehu, and L. M. Liberty (2000). New aeromagnetic data reveal large strike-

slip (?) faults in the northern Willamette Valley, Oregon, *Geol. Soc. Am. Bull.* **112,** no. 8, 1225–1233.

Blakely, R. J., R. E. Wells, C. S. Weaver, and S. Y. Johnson (2002). Location, structure, and seismicity of the Seattle fault zone, Washington: Evidence from aeromagnetic anomalies, geologic mapping, and seismic-reflection data, *Geol. Soc. Am. Bull.* **114,** no. 2, 169–177.

Blyth, H. E. (1997). The Quaternary geology of southeastern Vancouver Island, British Columbia, *Master's Thesis*, University of Alberta, Edmonton, Canada.

Boulton, G. S. (1971). Till genesis and fabric in Svalbard, Spitsbergen, *Till: A symposium*, Ohio State University Press Columbus, 41–72.

Boulton, G. S., and P. Caban (1995). Groundwater flow beneath ice sheets: Part II–Its impact on glacier tectonic structures and moraine formation, *Quaternary Sci. Rev.* **14,** no. 6, 563–587.

Bovis, M. J. (1982). Uphill-facing (antislope) scarps in the Coast Mountains, southwest British Columbia, *Geol. Soc. Am. Bull.* **93,** no. 8, 804–812.

Brandenberg, S. J., P. Wang, C. C. Nweke, K. Hudson, S. Mazzoni, Y. Bozorgnia, K. W. Hudnut, C. A. Davis, S. K. Ahdi, F. Zareian, *et al.* (2019). Preliminary report on engineering and geological effects of the July 2019 Ridgecrest earthquake sequence, *Tech. Rept.*, Geotechnical Extreme Event Reconnaissance Association, 1–69.

Brandon, M. T., and A. R. Calderwood (1990). High-pressure metamorphism and uplift of the Olympic subduction complex, *Geology* **18,** no. 12, 1252–1255.

Brandon, M. T., M. K. Roden-Tice, and J. I. Garver (1998). Late Cenozoic exhumation of the Cascadia accretionary wedge in the Olympic Mountains, northwest Washington State, *Geol. Soc. Am. Bull.* **110,** no. 8, 985–1009.

Bray, J. D., R. B. Seed, L. S. Cluff, and H. B. Seed (1994). Earthquake fault rupture propagation through soil, *J. Geotech. Eng.* **120,** no. 3, 543–561.

Brocher, T. M., T. Parsons, R. J. Blakely, M. A. Fisher, R. E. Wells, and N. I. Christensen (2001). Upper crustal structure in Puget Lowland, Washington-Results from the 1998 Seismic Hazards investigation in Puget Sound, *J. Geophys. Res.* **106,** no. B7, 13.

Brocher, T. M., R. E. Wells, A. P. Lamb, and C. S. Weaver (2017). Evidence for distributed clockwise rotation of the crust in the northwestern United States from fault geometries and focal mechanisms, *Tectonics* **36,** no. 5, 787–818.

Bronk Ramsey, C. (2017). OxCal Program, Version 4.3, available at https://c14.arch.ox.ac.uk/oxcal/OxCal.html (last accessed June 2020).

Brooks, B. A., S. E. Minson, C. L. Glennie, J. M. Nevitt, T. Dawson, R. Rubin, T. L. Ericksen, D. Lockner, K. Hudnut, V. Langenheim, *et al.* (2017). Buried shallow fault slip from the South Napa earthquake revealed by near-field geodesy, *Sci. Adv.* **3,** no. 7, e1700525, doi: 10.1126/sciadv.1700525.

Burbank, D. W., and R. S. Anderson (2011). *Tectonic Geomorphology*, John Wiley & Sons, Chichester, West Sussex, United Kingdom.

Cardozo, N., and R. W. Allmendinger (2013). Spherical projections with OSXStereonet, *Comput. Geosci.* **51,** 193–205.

Carol, H. (1947). The formation of Roches Moutonnées, *J. Glaciol.* **1,** no. 2, 57–59.

Carr, S., and J. Rose (2003). Till fabric patterns and significance: Particle response to subglacial stress, *Quaternary Sci. Rev.* **22,** no. 14, 1415–1426.

Chen, Y.-G., W.-S. Chen, J.-C. Lee, Y.-H. Lee, C.-T. Lee, H.-C. Chang, and C.-H. Lo (2001). Surface rupture of 1999 Chi-Chi earthquake yields insights on active tectonics of central Taiwan, *Bull. Seismol. Soc. Am.* **91,** no. 5, 977–985.

Chlieh, M., J.-P. Avouac, K. Sieh, D. H. Natawidjaja, and J. Galetzka (2008). Heterogeneous coupling of the Sumatran megathrust constrained by geodetic and paleogeodetic measurements, *J. Geophys. Res.* **113,** no. B5, doi: 10.1029/2007JB004981.

Cladouhos, T. T. (1999). Shape preferred orientations of survivor grains in fault gouge, *J. Struct. Geol.* **21,** no. 4, 419–436.

Clague, J. J., and T. S. James (2002). History and isostatic effects of the last ice sheet in southern British Columbia, *Quaternary Sci. Rev.* **21,** nos. 1/3, 71–87.

Clague, J. J., and B. Ward (2011). Pleistocene glaciation of British Columbia, in *Developments in Quaternary Sciences*, J. Ehlers, P. Gibbard, and P. Hughes (Editors), Vol. 15, Elsevier, Amsterdam, the Netherlands, 563–573.

Clowes, R. M., M. T. Brandon, A. G. Green, C. J. Yorath, A. S. Brown, E. R. Kanasewich, and C. Spencer (1987). LITHOPROBE–southern Vancouver Island: Cenozoic subduction complex imaged by deep seismic reflections, *Can. J. Earth Sci.* **24,** no. 1, 31–51.

Coppersmith, K. J., and R. R. Youngs (2000). Data needs for probabilistic fault displacement hazard analysis, *J. Geodyn.* **29,** nos. 3/5, 329–343.

Craig, T., E. Calais, L. Fleitout, L. Bollinger, and O. Scotti (2016). Evidence for the release of long-term tectonic strain stored in continental interiors through intraplate earthquakes, *Geophys. Res. Lett.* **43,** no. 13, 6826–6836.

Davenport, C. A., P. S. Ringrose, A. Becker, P. Hancock, and C. Fenton (1989). Geological investigations of late and post glacial earthquake activity in Scotland, in *Earthquakes at North-Atlantic Passive Margins: Neotectonics and Postglacial Rebound*, S. Gregersen and P. W. Basham (Editors), Springer, Dordretch, the Netherlands, 175–194.

Delano, J. E., R. D. Gold, R. W. Briggs, and R. W. Jibson (2018). Coseismic Sackungen in the New Madrid seismic zone, USA, *Geophys. Res. Lett.* **45,** no. 24, 13–258.

DeMets, C., R. G. Gordon, and D. F. Argus (2010). Geologically current plate motions, *Geophys. J. Int.* **181,** no. 1, 1–80.

Donath, F. A., and R. B. Parker (1964). Folds and folding, *Geol. Soc. Am. Bull.* **75,** no. 1, 45–62.

Dowdeswell, J. A., and M. J. Sharp (1986). Characterization of pebble fabrics in modern terrestrial glacigenic sediments, *Sedimentology* **33,** no. 5, 699–710.

Eddy, M. P., K. P. Clark, and M. Polenz (2017). Age and volcanic stratigraphy of the Eocene Siletzia oceanic plateau in Washington and on Vancouver Island, *Lithosphere* **9,** no. 4, 652–664.

England, T. D. J., L. D. Currie, N. W. D. Massey, M. K. Roden-Tice, and D. S. Miller (1997). Apatite fission-track dating of the Cowichan fold and thrust system, southern Vancouver Island, British Columbia, *Can. J. Earth Sci.* **34,** no. 5, 635–645.

Evans, D. J. A., E. R. Phillips, J. F. Hiemstra, and C. A. Auton (2006). Subglacial till: Formation, sedimentary characteristics and classification, *Earth Sci. Rev.* **78,** nos. 1/2, 115–176.

Evans, I. S. (1996). Abraded rock landforms (whalebacks) developed under ice streams in mountain areas, *Ann. Glaciol.* **22,** 9–16.

Fairchild, L. H., and D. S. Cowan (1982). Structure, petrology, and tectonic history of the Leech River complex northwest of Victoria, Vancouver Island, *Can. J. Earth Sci.* **19,** no. 9, 1817–1835.

Finley, T., K. Morell, L. Leonard, C. Regalla, S. T. Johnston, and W. Zhang (2019). Ongoing oroclinal bending in the Cascadia forearc and its relation to concave-outboard plate margin geometry, *Geology* **47,** no. 2, 155–158.

Fossen, H. (2016). *Structural Geology*, Cambridge University Press, Cambridge, United Kingdom.

Gallen, S. F., K. W. Wegmann, D. R. Bohnenstiehl, F. J. Pazzaglia, M. T. Brandon, and C. Fassoulas (2014). Active simultaneous uplift and margin-normal extension in a forearc high, Crete, Greece, *Earth Planet. Sci. Lett.* **398,** 11–24.

Gold, P. O., M. E. Oskin, A. J. Elliott, A. Hinojosa-Corona, M. H. Taylor, O. Kreylos, and E. Cowgill (2013). Coseismic slip variation assessed from terrestrial LiDAR scans of the El Mayor–Cucapah surface rupture, *Earth Planet. Sci. Lett.* **366,** 151–162.

Graham, A. (2018). Geometry, kinematics, and Quaternary activity of the brittle Leech River fault zone, southern Vancouver Island, British Columbia, Canada, *Master's Thesis*, University of Victoria, Victoria, Canada.

Greene, H. G., J. V. Barrie, and B. J. Todd (2018). The Skipjack Island fault zone: An active transcurrent structure within the upper plate of the Cascadia subduction complex, *Sediment. Geol.* **378,** 61–79.

Halchuk, S., J. E. Allen, and T. Onur (2019). Contribution of the Leech River-Devil's Mountain fault system to seismic hazard in Victoria, B.C., *Paper Presented at the 12th Canadian Conference on Earthquake Engineering*, Quebec City, Quebec, June 2019.

Ham, N. R., and D. M. Mickelson (1994). Basal till fabric and deposition at Burroughs glacier, Glacier Bay, Alaska, *Geol. Soc. Am. Bull.* **106,** no. 12, 1552–1559.

Hammer, Ø., D. A. T. Harper, and P. D. Ryan (2001). PAST: Paleontological statistics software package for education and data analysis, *Palaeontologia Electronica* **4,** no. 1, 9.

Hippolyte, J.-C., G. Brocard, M. Tardy, G. Nicoud, D. Bourlès, R. Braucher, G. Ménard, and B. Souffaché (2006). The recent fault scarps of the Western Alps (France): Tectonic surface ruptures or gravitational Sackung scarps? A combined mapping, geomorphic, levelling, and 10Be dating approach, *Tectonophysics* **418,** nos. 3/4, 255–276.

Hollingsworth, J., J. Jackson, R. Walker, M. Reza Gheitanchi, and M. Javad Bolourchi (2006). Strike-slip faulting, rotation, and along-strike elongation in the Kopeh Dagh mountains, NE Iran, *Geophys. J. Int.* **166,** no. 3, 1161–1177.

Hooyer, T. S., and N. R. Iverson (2000). Clast-fabric development in a shearing granular material: Implications for subglacial till and fault gouge, *Geol. Soc. Am. Bull.* **112,** no. 5, 683–692.

James, T., J. Bednarski, G. Rogers, and R. Currie (2010). LIDAR and digital aerial imagery of the Leech River Fault Zone and coastal regions from Sombrio Point to ten mile point, southern Vancouver Island, British Columbia, *Geol. Surv. Canada Open File 6211*, doi: 10.4095/285486.

Jarman, D., and C. K. Ballantyne (2002). Beinn Fhada, Kintail: An example of large-scale paraglacial rock slope deformation, *Scot. Geogr. J.* **118,** no. 1, 59–68.

Johnson, S. Y., S. V. Dadisman, J. R. Childs, and W. D. Stanley (1999). Active tectonics of the Seattle fault and central Puget Sound, Washington Implications for earthquake hazards, *Geol. Soc. Am. Bull.* **111,** no. 7, 1042–1053.

Johnson, S. Y., S. V. Dadisman, D. C. Mosher, R. J. Blakely, and J. R. Childs (2001). Active tectonics of the Devils Mountain fault and related structures, northern Puget Lowland and eastern Strait of Juan de Fuca region, Pacific Northwest, *U.S. Geol. Surv. Profess. Pap. 1643*, 46 pp., 2 plates.

Johnson, S. Y., C. J. Potter, and J. M. Armentrout (1994). Origin and evolution of the Seattle fault and Seattle basin, Washington, *Geology* **22,** no. 1, 71–74.

Johnson, S. Y., C. J. Potter, J. J. Miller, J. M. Armentrout, C. Finn, and C. S. Weaver (1996). The southern Whidbey Island fault: An active structure in the Puget Lowland, Washington, *Geol. Soc. Am. Bull.* **108,** no. 3, 334–354.

Johnston, S. T., and S. Acton (2003). The Eocene Southern Vancouver Island Orocline a response to seamount accretion and the cause of fold-and-thrust belt and extensional basin formation, *Tectonophysics* **365,** no. 1, 165–183.

Khazaradze, G., A. Qamar, and H. Dragert (1999). Tectonic deformation in western Washington from continuous GPS measurements, *Geophys. Res. Lett.* **26,** no. 20, 3153–3156.

Krüger, J. (1979). Structures and textures in till indicating subglacial deposition, *Boreas* **8,** no. 3, 323–340.

Kukovica, J., H. Ghofrani, S. Molnar, and K. Assatourians (2019). Probabilistic seismic hazard analysis of Victoria, British Columbia: Considering an active fault zone in the Nearby Leech River Valley, *Bull. Seismol. Soc. Am.* **109,** no. 5, 2050–2062.

Lagerbäck, R. (1990). Late Quaternary faulting and paleoseismicity in northern Fennoscandia, with particular reference to the Lansjärv area, northern Sweden, *Geologiska Föreningen i Stockholm Förhandlingar* **112,** no. 4, 333–354.

Lewis, W. V. (1954). Pressure release and glacial erosion, *J. Glaciol.* **2,** no. 16, 417–422.

Li, G., Y. Liu, C. Regalla, and K. D. Morell (2018). Seismicity relocation and fault structure near the Leech River Fault Zone, southern Vancouver Island, *J. Geophys. Res.* **123,** no. 4, 2841–2855.

Lienkaemper, J. J., and C. B. Ramsey (2009). OxCal: Versatile tool for developing paleoearthquake chronologies—A primer, *Seismol. Res. Lett.* **80,** no. 3, 431–434.

Lin, A., J. Guo, and B. Fu (2004). Co-seismic mole track structures produced by the 2001 Ms 8.1 Central Kunlun earthquake, China, *J. Struct. Geol.* **26,** no. 8, 1511–1519.

Lin, A., and M. Nishikawa (2011). Riedel shear structures in the co-seismic surface rupture zone produced by the 2001 Mw 7.8 Kunlun earthquake, northern Tibetan plateau, *J. Struct. Geol.* **33,** no. 9, 1302–1311.

Lin, A., G. Rao, D. Jia, X. Wu, B. Yan, and Z. Ren (2011). Co-seismic strike-slip surface rupture and displacement produced by the 2010 Mw 6.9 Yushu earthquake, China, and implications for Tibetan tectonics, *J. Geodyn.* **52,** nos. 3/4, 249–259.

MacLeod, N. S., D. L. Tiffin, P. D. Snavely Jr, and R. G. Currie (1977). Geologic interpretation of magnetic and gravity anomalies in the Strait of Juan de Fuca, US–Canada, *Can. J. Earth Sci.* **14,** no. 2, 223–238.

Massey, N. W. D., D. G. MacIntyre, P. J. Desjardins, and R. T. Cooney (2005). Digital geology map of British Columbia, *BC Ministry of Energy and Mines, Geofile, 7, 2005*.

Mazzotti, S., H. Dragert, J. Henton, M. Schmidt, R. Hyndman, T. James, Y. Lu, and M. Craymer (2003). Current tectonics of northern Cascadia from a decade of GPS measurements, *J. Geophys. Res.* **108,** no. B12, doi: 10.1029/2003JB002653.

Mazzotti, S., H. Dragert, R. D. Hyndman, M. M. Miller, and J. A. Henton (2002). GPS deformation in a region of high crustal seismicity: N. Cascadia forearc, *Earth Planet. Sci. Lett.* **198,** no. 1, 41–48.

Mazzotti, S., L. J. Leonard, J. F. Cassidy, G. C. Rogers, and S. Halchuk (2011). Seismic hazard in western Canada from GPS strain rates versus earthquake catalog, *J. Geophys. Res.* **116,** no. B12, doi: 10.1029/2011JB008213.

McCaffrey, R., A. I. Qamar, R. W. King, R. Wells, G. Khazaradze, C. A. Williams, C. W. Stevens, J. J. Vollick, and P. C. Zwick (2007). Fault locking, block rotation and crustal deformation in the Pacific Northwest, *Geophys. J. Int.* **169,** no. 3, 1315–1340.

McCalpin, J. P. (1999). Criteria for determining the seismic significance of sackungen and other scarplike landforms in mountainous regions, in *Techniques for Identifying Faults and Determining their Origins*, US Nuclear Regulatory Commission, Washington, 2–55.

McCalpin, J. P. (2009). *Paleoseismology*, Academic press, New York, New York.

McCalpin, J. P., and J. R. Irvine (1995). Sackungen at the Aspen Highlands ski area, Pitkin County, Colorado, *Environ. Eng. Geosci.* **1,** no. 3, 277–290.

McCrory, P. A., J. L. Blair, F. Waldhauser, and D. H. Oppenheimer (2012). Juan de Fuca slab geometry and its relation to Wadati-Benioff zone seismicity, *J. Geophys. Res.* **117,** no. B9, doi: 10.1029/2012JB009407.

Michel, L., T. A. Ehlers, C. Glotzbach, B. A. Adams, and K. Stübner (2018). Tectonic and glacial contributions to focused exhumation in the Olympic Mountains, Washington, USA, *Geology* **46,** no. 6, 491–494.

Miller, M. M., D. J. Johnson, C. M. Rubin, H. Dragert, K. Wang, A. Qamar, and C. Goldfinger (2001). GPS-determination of along-strike variation in Cascadia margin kinematics: Implications for relative plate motion, subduction zone coupling, and permanent deformation, *Tectonics* **20,** no. 2, 161–176.

Morell, K. D., T. W. Gardner, D. M. Fisher, B. D. Idleman, and H. M. Zellner (2013). Active thrusting, landscape evolution, and late Pleistocene sector collapse of Barú Volcano above the Cocos-Nazca slab tear, southern Central America, *Bulletin* **125,** nos. 7/8, 1301–1318.

Morell, K. D., C. Regalla, C. Amos, S. Bennett, L. Leonard, A. Graham, T. Reedy, V. Levson, and A. Telka (2018). Holocene surface rupture history of an active forearc fault redefines seismic hazard in southwestern British Columbia, Canada, *Geophys. Res. Lett.* **45,** no. 21, 11,605–11,611.

Morell, K. D., C. Regalla, L. J. Leonard, C. Amos, and V. Levson (2017). Quaternary rupture of a crustal fault beneath Victoria, British Columbia, Canada, *GSA Today* **27,** nos. 3/4, 4–10.

Muir-Wood, R. M. (1989). Extraordinary deglaciation reverse faulting in northern Fennoscandia, in *Earthquakes at North-Atlantic Passive Margins: Neotectonics and Postglacial Rebound*, S. Gregersen and P. W. Basham (Editors), Springer, Dordretch, the Netherlands, 141–173.

Muller, J. E. (1977). Evolution of the Pacific Margin, Vancouver Island, and adjacent regions, *Can. J. Earth Sci.* **14,** no. 9, 2062–2085.

Nelson, A. R., S. Y. Johnson, H. M. Kelsey, R. E. Wells, B. L. Sherrod, S. K. Pezzopane, L.-A. Bradley, R. D. Koehler, and R. C. Bucknam (2003). Late Holocene earthquakes on the Toe Jam Hill fault, Seattle fault zone, Bainbridge Island, Washington, *Geol. Soc. Am. Bull.* **115,** no. 11, 1388–1403.

Nelson, A. R., S. F. Personius, R. E. Wells, E. R. Schermer, L.-A. Bradley, J. Buck, and N. Reitman (2017). Holocene earthquakes of Magnitude 7 during westward escape of the Olympic Mountains, Washington, *Bull. Seismol. Soc. Am.* **107,** no. 5, 2394–2415.

Paterson, T. W., and G. Basque (2006). *Ghost Towns & Mining Camps of Vancouver Island*, Heritage House Publishing Co, Victoria, Canada.

Pazzaglia, F. J., and M. T. Brandon (2001). A fluvial record of long-term steady-state uplift and erosion across the Cascadia forearc high, western Washington State, *Am. J. Sci.* **301,** nos. 4/5, 385–431.

Personius, S. F., R. W. Briggs, A. R. Nelson, E. R. Schermer, J. Z. Maharrey, B. L. Sherrod, S. A. Spaulding, and L.-A. Bradley (2014). Holocene earthquakes and right-lateral slip on the left-lateral Darrington–Devils Mountain fault zone, northern Puget Sound, Washington, *Geosphere* **10,** no. 6, 1482–1500.

Petersen, M. D., T. E. Dawson, R. Chen, T. Cao, C. J. Wills, D. P. Schwartz, and A. D. Frankel (2011). Fault displacement hazard for strike-slip faults, *Bull. Seismol. Soc. Am.* **101,** no. 2, 805–825.

Philip, H., and M. Meghraoui (1983). Structural analysis and interpretation of the surface deformations of the El Asnam earthquake of October 10, 1980, *Tectonics* **2,** no. 1, 17–49.

Prothero, D. R., E. Draus, T. C. Cockburn, and E. A. Nesbitt (2008). Paleomagnetism and counterclockwise tectonic rotation of the Upper Oligocene Sooke Formation, southern Vancouver island, British Columbia, *Can. J. Earth Sci.* **45,** no. 4, 499–507.

Quigley, M., R. Van Dissen, N. Litchfield, P. Villamor, B. Duffy, D. Barrell, K. Furlong, T. Stahl, E. Bilderback, and D. Noble (2012). Surface rupture during the 2010 Mw 7.1 Darfield (Canterbury) earthquake: Implications for fault rupture dynamics and seismic-hazard analysis, *Geology* **40,** no. 1, 55–58.

Rao, G., A. Lin, B. Yan, D. Jia, X. Wu, and Z. Ren (2011). Co-seismic Riedel shear structures produced by the 2010 Mw 6.9 Yushu earthquake, central Tibetan Plateau, China, *Tectonophysics* **507,** nos. 1/4, 86–94.

Reimer, P. J., E. Bard, A. Bayliss, J. W. Beck, P. G. Blackwell, C. B. Ramsey, C. E. Buck, H. Cheng, R. L. Edwards, M. Friedrich, *et al.* (2013). IntCal13 and Marine13 radiocarbon age calibration curves 0–50,000 years cal BP, *Radiocarbon* **55,** no. 4, 1869–1887.

Reitman, N. G., S. E. K. Bennett, R. D. Gold, R. W. Briggs, and C. B. DuRoss (2015). High-resolution trench photomosaics from image-based modeling: Workflow and error analysis, *Bull. Seismol. Soc. Am.* **105,** no. 5, 2354–2366.

Reitman, N. G., K. J. Mueller, G. E. Tucker, R. D. Gold, R. W. Briggs, and K. R. Barnhart (2019). Offset channels may not accurately record strike-slip fault displacement: Evidence from landscape evolution models, *J. Geophys. Res.***124,** no. 12, 13,427–13,451.

Rijsdijk, K. F., G. Owen, W. P. Warren, D. McCarroll, and J. J. M. van der Meer (1999). Clastic dykes in over-consolidated tills: evidence for subglacial hydrofracturing at Killiney Bay, eastern Ireland, *Sediment. Geol.* **129,** nos. 1/2, 111–126.

Saillard, M., L. Audin, B. Rousset, J.-P. Avouac, M. Chlieh, S. R. Hall, L. Husson, and D. L. Farber (2017). From the seismic cycle to long-term deformation: Linking seismic coupling and Quaternary coastal geomorphology along the Andean megathrust, *Tectonics* **36,** no. 2, 241–256.

Sanderson, D. J., and W. R. D. Marchini (1984). Transpression, *J. Struct. Geol.* **6,** no. 5, 449–458.

Savard, G., M. G. Bostock, and N. I. Christensen (2018). Seismicity, metamorphism, and fluid evolution across the Northern Cascadia fore arc, *Geochem. Geophys. Geosys.* **19,** no. 6, 1881–1897.

Schermer, E. R., C. B. Amos, W. C. Duckworth, A. R. Nelson, S. Angster, J. Delano, and B. L. Sherrod (2020). Postglacial Mw 7.0–7.5 earthquakes on the North Olympic Fault Zone, Washington, *Bull. Seismol. Soc. Am.* early Publication.

Sherrod, B. L., E. Barnett, E. Schermer, H. M. Kelsey, J. Hughes, F. F. Foit, C. S. Weaver, R. Haugerud, and T. Hyatt (2013). Holocene tectonics and fault reactivation in the foothills of the north Cascade Mountains, Washington, *Geosphere* **9,** no. 4, 827–852, GES00,880–1.

Sherrod, B. L., R. J. Blakely, C. S. Weaver, H. M. Kelsey, E. Barnett, L. Liberty, K. L. Meagher, and K. Pape (2008). Finding concealed active faults: Extending the southern Whidbey Island fault across the Puget Lowland, Washington, *J. Geophys. Res.* **113,** no. B5, doi: 10.1029/2007JB005060.

Sherrod, B. L., T. M. Brocher, C. S. Weaver, R. C. Bucknam, R. J. Blakely, H. M. Kelsey, A. R. Nelson, and R. Haugerud (2004). Holocene fault scarps near Tacoma, Washington, USA, *Geology* **32,** no. 1, 9–12.

Sitchler, J. C., D. M. Fisher, T. W. Gardner, and M. Protti (2007). Constraints on inner forearc deformation from balanced cross sections, Fila Costeña thrust belt, Costa Rica, *Tectonics* **26,** no. 6, doi: 10.1029/2006TC001949.

Stirling, M., T. Goded, K. Berryman, and N. Litchfield (2013). Selection of earthquake scaling relationships for seismic-hazard analysis, *Bull. Seismol. Soc. Am.* **103,** no. 6, 2993–3011.

Stuiver, M., and P. J. Reimer (1993). Extended 14 C data base and revised CALIB 3.0 14 C age calibration program, *Radiocarbon* **35,** no. 1, 215–230.

Sylvester, A. G. (1988). Strike-slip faults, *Geol. Soc. Am. Bull.* **100,** no. 11, 1666–1703.

Thomason, J. F., and N. R. Iverson (2006). Microfabric and microshear evolution in deformed till, *Quaternary Sci. Rev.* **25,** nos. 9/10, 1027–1038.

Thompson, S. C., R. J. Weldon, C. M. Rubin, K. Abdrakhmatov, P. Molnar, and G. W. Berger (2002). Late Quaternary slip rates across the central Tien Shan, Kyrgyzstan, central Asia, *J. Geophys. Res.* **107,** no. B9, ETG–7.

Thorson, R. M. (2000). Glacial tectonics: A deeper perspective, *Quaternary Sci. Rev.* **19,** nos. 14/15, 1391–1398.

Toda, S., H. Kaneda, S. Okada, D. Ishimura, and Z. K. Mildon (2016). Slip-partitioned surface ruptures for the Mw 7.0 16 April 2016 Kumamoto, Japan, earthquake, *Earth Planets Space* **68,** no. 1, 188.

Van Der Meer, J. J. M., K. H. Kjaer, and J. Krüger (1999). Subglacial water-escape structures and till structures, Sléttjökull, Iceland, *J. Quaternary Sci.* Published for the Quaternary Research Association, **14,** no. 3, 191–205.

Walsh, T. J., and R. L. Logan (2007). Field data for a trench on the Canyon River fault, southeast Olympic Mountains, Washington, *Open-File Rept. Wash. Div. Geol. Earth Resour. 2007-1 0731-7492*, 1 pp.

Walsh, T. J., R. L. Logan, and K. G. Neal (1997).The Canyon River fault, an active fault in the southern Olympic Range, Washington, *Washington Geol.* **25,** no. 4, 21–24.

Wang, K., L. Brown, Y. Hu, K. Yoshida, J. He, and T. Sun (2019). Stable forearc stressed by a weak megathrust: Mechanical and geodynamic implications of stress changes caused by the M= 9 Tohoku-oki earthquake, *J. Geophys. Res.* **124,** no. 6, 6179–6194.

Wang, K., R. Wells, S. Mazzotti, R. D. Hyndman, and T. Sagiya (2003). A revised dislocation model of interseismic deformation of the Cascadia subduction zone, *J. Geophys. Res.* **108,** no. B1, doi: 10.1029/2001JB001227.

Weinberger, R. (2014). Pleistocene strain partitioning during transpression along the Dead Sea Transform, Metulla Saddle, northern Israel, in *Dead Sea Transform Fault System: Reviews*, Z. Garfunkel, Z. Ben-Avraham, and E. Kagan (Editors), Springer, Dordrecht, the Netherlands, 151–182.

Wells, R. E., R. J. Blakely, and S. Bemis (2020). Northward migration of the Oregon forearc on the Gales Creek fault, *Geosphere* **16,** no. 2, 660–684.

Wells, R. E., R. J. Blakely, Y. Sugiyama, D. W. Scholl, and P. A. Dinterman (2003). Basin-centered asperities in great subduction zone earthquakes: A link between slip, subsidence, and subduction erosion?, *J. Geophys. Res.* **108,** no. B10, doi: 10.1029/2002JB002072.

Wells, R. E., and R. McCaffrey (2013). Steady rotation of the Cascade arc, *Geology* **41,** no. 9, 1027–1030.

Wells, R. E., C. S. Weaver, and R. J. Blakely (1998). Fore-arc migration in Cascadia and its neotectonic significance, *Geology* **26,** no. 8, 759–762.

Wesnousky, S. G. (2008). Displacement and geometrical characteristics of earthquake surface ruptures: Issues and implications for seismic-hazard analysis and the process of earthquake rupture, *Bull. Seismol. Soc. Am.* **98,** no. 4, 1609–1632.

Wilcox, R. E., T. P. Harding, and D. Seely (1981). Basic wrench tectonics, *Am. Assoc. Petrol. Geol. Bull.* **57,** 74–96.

Wilson, J. R., M. J. Bartholomew, and R. J. Carson (1979). Late Quaternary faults and their relationship to tectonism in the Olympic Peninsula, Washington, *Geology* **7,** no. 5, 235–239.

Witter, R. C., R. W. Givler, and R. J. Carson (2008). Two post-glacial earthquakes on the Saddle Mountain West fault, southeastern Olympic Peninsula, Washington, *Bull. Seismol. Soc. Am.* **98,** no. 6, 2894–2917.

Woodcock, N. H., and M. Fischer (1986). Strike-slip duplexes, *J. Struct. Geol.* **8,** no. 7, 725–735.

Woodcock, N. H., and B. Rickards (2003). Transpressive duplex and flower structure: Dent fault system, NW England, *J. Struct. Geol.* **25,** no. 12, 1981–1992.

Youngs, R. R., W. J. Arabasz, R. E. Anderson, A. R. Ramelli, J. P. Ake, D. B. Slemmons, J. P. McCalpin, D. I. Doser, C. J. Fridrich, F. H. Swan III, *et al.* (2003). A methodology for probabilistic fault displacement hazard analysis (PFDHA), *Earthq. Spectra* **19,** no. 1, 191–219.

Zachariasen, J., and K. Sieh (1995). The transfer of slip between two en echelon strike-slip faults: A case study from the 1992 Landers earthquake, southern California, *J. Geophys. Res.* **100,** no. B8, 15,281–15,301.

Zielke, O. (2018). Earthquake recurrence and the resolution potential of tectono-geomorphic records, *Bull. Seismol. Soc. Am.* **108,** no. 3A, 1399–1413.

APPENDIX

The Appendix section contains the datasets (Tables A1–A6) used for the analyses of glacial flow direction and till clast orientations.

TABLE A1
Glacial Flow Indicator Types, Locations, and Azimuths

Feature Type*	Start Easting†	Start Northing	End Easting	End Northing	Azimuth
Map-scale groove	446,196	5,371,271	446,155	5,371,151	197
Streamlined ridge	446,441	5,371,308	446,371	5,371,119	198
Streamlined ridge	446,566	5,370,880	446,448	5,370,615	202
Drumlin	449,709	5,370,043	449,661	5,369,731	186
Streamlined ridge	448,953	5,370,540	448,893	5,370,252	189
Streamlined ridge	448,860	5,370,510	448,816	5,370,279	188
Streamlined ridge	448,916	5,370,191	448,871	5,370,054	196
Streamlined ridge	449,329	5,370,290	449,249	5,370,069	198
Streamlined ridge	447,825	5,370,568	447,723	5,370,267	196
Bedrock drumlin	448,514	5,369,841	448,461	5,369,692	197
Map-scale groove	448,853	5,369,949	448,811	5,369,867	205
Streamlined ridge	449,146	5,369,805	449,109	5,369,705	198
Roche moutonée	449,783	5,370,074	449,764	5,369,956	191
Drumlin	449,662	5,369,715	449,640	5,369,578	187
Streamlined ridge	450,080	5,369,755	450,060	5,369,596	185
Bedrock drumlin	450,174	5,369,746	450,152	5,369,675	195
Bedrock drumlin	450,153	5,369,626	450,151	5,369,566	179
Bedrock drumlin	450,267	5,369,645	450,238	5,369,565	197
Map-scale groove	449,745	5,369,578	449,734	5,369,527	191
Map-scale groove	450,127	5,369,466	450,060	5,369,247	195
Streamlined ridge	450,016	5,369,497	449,972	5,369,420	208
Drumlin	451,236	5,370,694	451,168	5,370,312	188
Bedrock drumlin	448,677	5,369,987	448,651	5,369,935	204
Bedrock drumlin	448,845	5,370,020	448,823	5,369,970	201
Roche moutonée	446,092	5,371,455	446,082	5,371,407	190
Roche moutonée	446,116	5,371,428	446,104	5,371,375	190
Bedrock drumlin	445,932	5,371,434	445,910	5,371,369	197
Bedrock drumlin	445,998	5,371,425	445,984	5,371,388	198
Streamlined ridge	446,429	5,371,017	446,394	5,370,952	206
Streamlined ridge	449,264	5,369,680	449,204	5,369,534	200
Streamlined ridge	449,626	5,369,785	449,599	5,369,680	192
Streamlined ridge	449,025	5,370,103	448,985	5,370,006	200
Streamlined ridge	448,582	5,369,842	448,551	5,369,766	200
Streamlined ridge	450,031	5,369,739	450,014	5,369,611	185
Drumlin	453,287	5,369,889	453,257	5,369,615	184
Roche moutonée	441,161	5,372,397	441,123	5,372,333	209
Streamlined ridge	444,387	5,371,690	444,386	5,371,557	178
Bedrock drumlin	445,979	5,371,279	445,949	5,371,192	197
Roche mouton´ee	445,782	5,371,206	445,761	5,371,157	200
Map-scale groove	449,583	5,370,025	449,544	5,369,881	193
Drumlin	449,453	5,371,520	449,429	5,371,441	195

*Feature type interpreted from light detection and ranging (lidar).
†All coordinates are reported in NAD 83 BC Environment Albers NAD 83 UTM Zone 10.

TABLE A2
Plunge and Trend of Prolate Clasts in Undeformed Lodgment Till (Unit GH1) in the Good Hope Trench

Location*	Plunge	Trend	Clast Size†
5H–6H	30	077	C
5H–6H	20	012	P
5H–6H	22	055	P
5H–6H	21	023	C
5H–6H	5	180	P
5H–6H	10	143	P
5H–6H	39	053	P
5H–6H	4	189	P
5H–6H	34	045	P
5H–6H	10	175	C
5H–6H	4	173	P
5H–6H	2	173	P
5H–6H	9	042	C
5H–6H	7	255	P
5H–6H	17	032	P
5H–6H	13	026	P
5H–6H	19	088	P
5H–6H	4	210	P
5H–6H	26	347	P
5H–6H	8	060	P
5H–6H	49	035	P
5H–6H	21	078	P
5H–6H	10	257	P
5H–6H	7	235	P
5H–6H	18	235	P
6H–7H	38	084	P
6H–7H	27	308	P
6H–7H	9	047	P
6H–7H	25	305	P
6H–7H	37	000	P
6H–7H	11	129	P
6H–7H	35	042	P
6H–7H	30	111	C
6H–7H	38	106	P
6H–7H	38	060	P
6H–7H	25	080	P
6H–7H	5	258	P
6H–7H	15	019	C
6H–7H	7	025	C
6H–7H	23	356	P
6H–7H	20	180	P
6H–7H	8	050	P
6H–7H	18	054	P
6H–7H	5	178	P
6H–7H	13	218	P
6H–7H	19	114	P
6H–7H	21	313	P
6H–7H	26	187	P
6H–7H	18	182	P
6H–7H	10	254	P

*Orientations were measured in both walls.
†P is pebble sized, and C is cobble sized.

TABLE A3
Plunge and Trend of Prolate Clasts in Faulted Lodgment Till in Faults B and C (Unit GH1) in the Good Hope Trench

Location	Plunge	Trend	Clast Size*
10H west	40	105	P
10H west	21	70	P
10H west	17	20	P
10H west	3	327	P
10H west	10	120	C
10H west	30	6	P
10H west	15	277	P
10H west	47	70	P
10H west	3	197	P
10H west	5	130	P
10H west	49	184	P
10H west	2	251	P
10H west	32	276	P
10H west	22	260	P
10H west	42	112	C
10H west	27	126	P
10H west	27	328	P
10H west	17	145	P
10H west	42	123	P
10H west	76	281	P
10H west	6	242	P
10H west	28	60	P
10H west	43	332	P
10H west	20	138	P
10H west	28	172	P
11H east	35	317	P
11H east	17	238	P
11H east	16	103	P
11H east	15	252	P
11H east	20	250	P
11H east	4	200	C
11H east	34	306	P
11H east	30	310	P
11H east	38	20	P
11H east	9	121	P
11H east	35	226	P
11H east	27	45	P
11H east	10	210	P
11H east	5	35	P
11H east	74	300	P
11H east	18	280	P
11H east	7	285	C
11H east	18	297	P
11H east	40	11	P
11H east	10	119	P
11H east	7	117	C
11H east	0	127	C
11H east	14	110	P
11H east	14	136	P
11H east	39	52	C

*P is pebble sized, and C is cobble sized.

TABLE A4
Plunge and Trend of Prolate Clasts in Faulted Lodgment Till in Fault A (Unit GH1) in the Good Hope Trench

Location	Plunge	Trend	Clast Size*
12H east	20	130	P
12H east	15	53	P
12H east	30	19	P
12H east	60	67	P
12H east	27	87	P
12H east	5	120	P
12H east	22	13	P
12H east	4	2	P
12H east	24	179	P
12H east	30	12	P
12H east	64	248	P
12H east	22	73	P
12H east	14	310	P
12H east	9	340	P
12H east	20	204	P
12H east	32	273	P
12H east	18	290	P
12H east	5	248	P
12H east	17	34	P
12H east	3	156	P
12H east	57	190	P
12H east	6	80	P
12H east	4	32	P
12H east	70	214	P
12H east	75	330	P

*P is pebble sized, and C is cobble sized.

TABLE A5
Orientations of *a*/*b* Planes of Oblate Clasts in Undeformed Meltout Till (Unit GH2) in the Good Hope Trench

Location	Strike	Dip	Dip Direction	Clast Size*
5H–6H west wall	334	55	North	Not recorded
5H–6H west wall	334	76	North	Not recorded
5H–6H west wall	11	57	East	Not recorded
5H–6H west wall	324	86	South	Not recorded
5H–6H west wall	302	90		Not recorded
5H–6H west wall	30	55	West	Not recorded
5H–6H west wall	5	42	East	Not recorded
5H–6H west wall	295	53	North	Not recorded
5H–6H west wall	345	55	Southwest	Not recorded
5H–6H west wall	302	46	North	Not recorded
5H–6H west wall	276	44	South	Not recorded
5H–6H west wall	240	52	South	C
5H–6H west wall	350	82	West	Not recorded
5H–6H west wall	328	74	Northeast	Not recorded
5H–6H west wall	252	61	North	Not recorded
5H–6H west wall	283	25	South	Not recorded
5H–6H west wall	311	57	North	P
5H–6H west wall	317	24	South	C
5H–6H west wall	5	67	East	P
5H–6H west wall	240	35	South	P
5H–6H west wall	252	55	South	P
5H–6H west wall	310	44	North	P
5H–6H west wall	327	19	North	P
5H–6H west wall	0	27	East	P
5H–6H west wall	255	72	South	C
5H–6H west wall	89	75	South	C
5H–6H west wall	347	27	East	C
5H–6H west wall	333	83	West	C
5H–6H west wall	336	29	North	P
6H–7H west wall	329	51	North	C
6H–7H west wall	312	33	North	P
6H–7H west wall	0	45	East	P
6H–7H west wall	6	30	East	C
6H–7H west wall	257	66	South	P
6H–7H west wall	320	58	North	C
6H–7H west wall	280	35	South	P
6H–7H west wall	300	24	North	C
6H–7H west wall	274	31	South	C
6H–7H west wall	290	20	South	P
6H–7H west wall	10	73	East	C
6H–7H west wall	272	17	North	P
6H–7H west wall	280	34	North	C
6H–7H west wall	220	35	Southeast	P
6H–7H west wall	321	35	North	P
6H–7H west wall	265	37	South	C
6H–7H west wall	252	34	South	P
6H–7H west wall	325	78	North	C
6H–7H west wall	324	80	North	P
6H–7H west wall	3	63	East	C
6H–7H west wall	54	28	East	P
6H–7H west wall	304	77	South	P
6H–7H west wall	346	38	East	C
6H–7H west wall	29	74	East	P
6H–7H west wall	234	32	South	C
6H–7H west wall	255	4	North	C

*P is pebble sized, and C is cobble sized.

TABLE A6
Orientations of *a*/*b* Planes of Oblate Clasts in Meltout Till (Unit GH2) above Fault B in the Good Hope Trench

Location	Strike	Dip	Dip Direction	Clast Size*
10H west	235	45	North	C
10H west	280	82	North	C
10H west	68	67	South	P
10H west	45	82	East	P
10H west	26	14	North	C
10H west	130	66	South	P
10H west	306	90		P
10H west	7	44	East	P
10H west	275	43	North	P
10H west	265	77	North	C
10H west	284	45	North	C
10H west	255	54	North	C

(*continued*)

TABLE A6 (*Continued*)

Location	Strike	Dip	Dip Direction	Clast Size*
10H west	284	79	North	P
10H west	334	24	Southwest	P
10H west	8	34	North	P
10H west	335	34	North	P
10H west	316	46	South	P
10H west	350	90		P
10H west	234	39	North	P
10H west	336	32	North	C
10H west	297	85	South	C
10H west	350	14	East	C
10H west	30	25	East	P
10H west	40	26	East	P
10H west	280	46	North	C
11H east	293	88	South	C
11H east	34	69	East	C
11H east	273	75	North	C
11H east	134	54	South	C
11H east	23	68	East	C
11H east	346	22	North	P
11H east	262	44	North	P
11H east	214	54	South	C
11H east	272	66	South	P

(*continued*)

TABLE A6 (*Continued*)

Location	Strike	Dip	Dip Direction	Clast Size*
11H east	173	56	East	C
11H east	355	61	West	C
11H east	283	69	North	P
11H east	161	43	North	C
11H east	215	43	North	P
11H east	121	73	South	P
11H east	92	82	South	P
11H east	34	21	West	C
11H east	32	72	East	C
11H east	240	64	North	C
11H east	246	72	North	P
11H east	316	32	South	P
11H east	170	90		P
11H east	272	53	North	P
11H east	132	36	South	C
11H east	134	77	South	P

*P is pebble sized, and C is cobble sized.

Manuscript received 10 June 2020
Published online 26 January 2021